THE STAR FORMATION RATE EFFICIENCY OF NEUTRAL ATOMIC-DOMINATED HYDROGEN GAS IN THE OUTSKIRTS OF STAR-FORMING GALAXIES FROM $z \sim 1$ TO $z \sim 3$

MARC RAFELSKI[1,7], JONATHAN P. GARDNER[1], MICHELE FUMAGALLI[2], MARCEL NEELEMAN[3], HARRY I. TEPLITZ[4], NORMAN GROGIN[5], ANTON M. KOEKEMOER[5], AND CLAUDIA SCARLATA[6]
[1] Goddard Space Flight Center, Code 665, Greenbelt, MD 20771, USA; marc.a.rafelski@nasa.gov
[2] Institute for Computational Cosmology and Centre for Extragalactic Astronomy, Department of Physics, Durham University, South Road, Durham DH1 3LE, UK
[3] Department of Astronomy & Astrophysics, UCO/Lick Observatory, 1156 High Street, University of California, Santa Cruz, CA 95064, USA
[4] Infrared Processing and Analysis Center, MS 100-22, Caltech, Pasadena, CA 91125, USA
[5] Space Telescope Science Institute, 3700 San Martin Drive, Baltimore, MD 21218, USA
[6] Minnesota Institute for Astrophysics, School of Physics and Astronomy, University of Minnesota, Minneapolis, MN 55455, USA
Received 2016 February 3; revised 2016 April 27; accepted 2016 April 27; published 2016 July 6

ABSTRACT

Current observational evidence suggests that the star formation rate (SFR) efficiency of neutral atomic hydrogen gas measured in damped Lyα systems (DLAs) at $z \sim 3$ is more than 10 times lower than predicted by the Kennicutt–Schmidt (KS) relation. To understand the origin of this deficit, and to investigate possible evolution with redshift and galaxy properties, we measure the SFR efficiency of atomic gas at $z \sim 1$, $z \sim 2$, and $z \sim 3$ around star-forming galaxies. We use new robust photometric redshifts in the Hubble Ultra Deep Field to create galaxy stacks in these three redshift bins, and measure the SFR efficiency by combining DLA absorber statistics with the observed rest-frame UV emission in the galaxies' outskirts. We find that the SFR efficiency of H I gas at $z > 1$ is $\sim$1%–3% of that predicted by the KS relation. Contrary to simulations and models that predict a reduced SFR efficiency with decreasing metallicity and thus with increasing redshift, we find no significant evolution in the SFR efficiency with redshift. Our analysis instead suggests that the reduced SFR efficiency is driven by the low molecular content of this atomic-dominated phase, with metallicity playing a secondary effect in regulating the conversion between atomic and molecular gas. This interpretation is supported by the similarity between the observed SFR efficiency and that observed in local atomic-dominated gas, such as in the outskirts of local spiral galaxies and local dwarf galaxies.

Key words: galaxies: evolution – galaxies: high-redshift – galaxies: photometry – galaxies: star formation – galaxies: structure – quasars: absorption lines

1. INTRODUCTION

The cold gas from which stars form is difficult to detect in emission at high redshift, and therefore it is generally studied in absorption to background quasars (QSOs), particularly with damped Lyα systems (DLAs), which have a minimum H I column density of 2×10^{20} cm^{-2}. DLAs are found to trace most of the neutral H I gas in the universe, containing enough gas to account for 50% of the mass content of visible matter in modern galaxies (Wolfe et al. 2005). In addition to studying the individual physical properties of absorbers, surveys of DLAs at high redshift have found that the comoving average H I mass density decreases by a factor of 2 from $z \sim 5$ to $z \sim 2$ (Prochaska & Wolfe 2009; Noterdaeme et al. 2012; Crighton et al. 2015; Sánchez-Ramírez et al. 2016) and the cosmic metallicity of the H I gas is observed to increase by a factor of 8 from $z \sim 5$ to $z \sim 1$ (Prochaska et al. 2003; Rafelski et al. 2012, 2014). Yet even with these advances we know little about the extent and size of the absorbing gas.

Simulations suggest that DLAs trace dense gas in and around galaxies (e.g., Nagamine et al. 2007; Pontzen et al. 2008; Tescari et al. 2009; Cen 2012; Bird et al. 2014). Measurements of the cross-correlation of the Lyα forest and DLAs find a large bias factor that implies host halo masses of DLAs as high as $\sim 10^{12}$ $M_\odot$ at $z > 2.15$ (Font-Ribera et al. 2012). At the same time, the cross-correlation of DLAs and Lyman break galaxies (LBGs) at $z \sim 3$ suggests host halo masses of $\sim 10^{11}$ $M_\odot$

---

[7] NASA Postdoctoral Program Fellow.

(Cooke et al. 2006). At $z \sim 3$, star-forming galaxies (SFGs) have halo masses of $\sim 10^{11.5}$ $M_\odot$ (Bielby et al. 2013), indicating that DLAs could be associated with typical or even massive SFGs.

Direct imaging of high-redshift DLAs has primarily failed due to a combination of intrinsically low star formation rates (SFRs) of the associated galaxies and the glare of the background QSO. The bright QSOs prevent searches for faint galaxy associations at $\lesssim 1''$ from the absorbing gas (e.g., Warren 2001). Therefore, despite almost 20 yr of observations, only about a dozen DLA host galaxies have been observed in emission (see Tables 1 and 2 in Krogager et al. 2012 and Fumagalli et al. 2015, respectively). Although these galaxies appear to be mostly typical SFGs (Møller 2002; Fynbo et al. 2010, 2013; Péroux et al. 2012; Bouché et al. 2013; Krogager et al. 2013; Jorgenson & Wolfe 2014), a publication bias exists due to a lack of census for nondetections and biased search criteria (e.g., targeting high-metallicity systems, and with sensitivities only sufficient to observe more luminous galaxies). Recently, Fumagalli et al. (2015) provided a full census not biased by metallicity and did not detect the host galaxies.

There are currently four other techniques available to investigate the in situ SFR of DLAs: (1) gamma-ray burst (GRB) observations, (2) the "double" DLA technique, (3) the C II* technique, and (4) a statistical comparison of absorbers with observed emission. In the next few paragraphs we will briefly describe these techniques.

The use of GRBs instead of QSOs to study DLAs is promising, as GRBs fade over time, enabling deep searches for emission from the DLAs without the bright nearby quasar. The majority of GRB-DLAs are not intervening, but rather are associated with the galaxies hosting the GRB. Therefore, GRB-DLAs will be biased with respect to their selection, as GRBs are related to supernova explosions within galaxies (e.g., Kumar & Zhang 2015), and therefore are a priori associated with SFGs. GRB-DLAs have slightly different physical properties than QSO-DLAs, such as a different metallicity evolution (Cucchiara et al. 2015), and only a small number of GRB-DLA sightlines have been studied, since the afterglows fade over time (Schulze et al. 2012).

The double DLA technique uses QSO sightlines containing two optically thick absorbers, with the higher-redshift system acting as a blocking filter for the lower-redshift source. One can then conduct a sensitive search for emission from the lower-redshift source, as the higher-redshift system blocks all light from the QSO (Steidel & Hamilton 1992; O'Meara et al. 2006; Fumagalli et al. 2010, 2014). An unbiased search for DLA host galaxies using this technique yielded no confirmed detections in a sample of 32 DLAs, and the stack of all measurements yielded an SFR limit of $\lesssim 0.3\,M_{\odot}\,{\rm yr}^{-1}$ within 2 kpc from the QSO position (Fumagalli et al. 2015).

The C II* technique is described in detail by Wolfe et al. (2003a, 2003b). In short, the technique relies on equating the cooling rate dominated by [C II] 158 μm cooling with the heating rate, set in part by the SFR. By measuring the C II* $\lambda 1335.7$ transition, the cooling rate ℓ_c can be calculated, which leads to an estimate of the SFR. However, the inferred SFRs from this measured for typical DLAs by Wolfe et al. (2008) may be in conflict with the results by Fumagalli et al. (2015), as they predict higher SFRs in the typical DLA population. Careful calibration of the technique is required with a sample of galaxies with known SFRs. Since the C II* $\lambda 1335.7$ absorption line arises from the same excited fine-structure state that gives rise to [C II] 158 μm emission, ALMA measurements of a sample of DLAs should help advance our understanding of C II* $\lambda 1335.7$.

The last technique, which is the one presented in this paper, relies on a statistical comparison to connect absorption-line studies tracing the gas, with SFGs measured in emission. It does so by predicting the comoving SFR density from DLAs by combining the column-density distribution function of H I gas at high redshift (e.g., Prochaska & Wolfe 2009) with the Kennicutt–Schmidt (KS) relation (Schmidt 1959; Kennicutt 1998b) and a geometrical model (Rafelski et al. 2011), and then compares this prediction to emission that likely originates from DLAs.

Since the expected emission from DLAs is below 29 mag arcsec^{-2} (Wolfe & Chen 2006), it is important to conduct any search for such emission in a very deep imaging field. We make this measurement in the Hubble Ultra Deep Field (UDF; Beckwith et al. 2006) because it is the only rest-frame UV imaging that has sufficient sensitivity and resolution to measure the SFR in emission at high redshift.

There are two possible locations to observe emission from DLAs at high redshift: either in isolated regions unassociated with SFGs, or in the outskirts of SFGs. A search for such emission in isolated regions of the UDF was conducted at $z \sim 3$ by Wolfe & Chen (2006). They assumed that all the emission was unassociated with SFGs, and found upper limits

on the SFR efficiency of $\sim 10\%$. This SFR efficiency is defined as the fractional decrease in the normalization of the KS relation, where $\sim 10\%$ is a factor of 10 decrease in the normalization.

Since DLAs are expected to be associated with SFGs, a search for emission was conducted by Rafelski et al. (2011) in the outskirts of $z \sim 3$ SFGs in the UDF. In order to obtain reliable photometric redshifts of SFGs, the Lyman break of the spectral energy distribution (SED) needed to be sampled. Galaxy redshifts were determined by both color selection and photometric redshifts, including ground-based u-band data sampling the Lyman break at $z \sim 3$ (Rafelski et al. 2009). The study found that if the emission in the outskirts of the SFGs is due to in situ star formation (SF) in atomic-dominated hydrogen gas, then the SFR efficiency of the gas at $z \sim 3$ is between $\sim 2\%$ and 10%.

There are multiple possible effects contributing to the lower SFR efficiencies than predicted by the KS relation, such as the lower metallicity of DLA H I gas (e.g., Gnedin & Kravtsov 2011), a higher background radiation field at high redshift (e.g., Haardt & Madau 2012), and the role of molecular versus atomic hydrogen gas in star formation (e.g., Glover & Clark 2012; Krumholz 2012, 2013; Michałowski et al. 2015). Measurements of the evolution of the SFR efficiency and metallicity over time will help distinguish between these different possibilities.

In order to measure the evolution in the SFR efficiency, we require accurate redshift estimates of SFGs. The newly observed UV imaging of the UDF (Teplitz et al. 2013) provides significantly improved redshifts at $z < 4$, and the new redshift catalog reduces the outlier fraction by a factor of ~ 3 (Rafelski et al. 2015). These high-fidelity redshifts and high-resolution UDF images can then be used to create stacks of galaxies at varying epochs enabling the measurement of the SFR efficiency of atomic-dominated H i gas in the outskirts of SFGs at $z \sim 1$ and $z \sim 2$ while also improving the $z \sim 3$ measurement.

A comparison of the SFR of high-redshift galaxies with the inferred molecular gas surface densities measured at $z \sim 1 - 3$ suggests little to no evolution compared to the the KS relation measured at $z = 0$ (Daddi et al. 2010; Genzel et al. 2010; Tacconi et al. 2010, 2013). While these studies have measured the efficiency of star formation at high redshift in molecular-dominated gas, they do not address the SFR efficiency for neutral atomic-dominated H i gas in the galaxy outskirts, as done in this study.

The outline of this paper is as follows. In Section 2 we analyze the data; we describe how we measure SFRs (2.1), define our galaxy samples (2.2), create composite stacks (2.3), extract radial surface brightness profiles (2.4), and consider the effects of Lyα on the profiles (2.5). In Section 3 we describe how we obtain the SFR efficiency; we determine the column-density distribution function of DLAs (3.1), measure the SFR efficiency (3.2), and visualize the efficiency on the KS plot (3.3). In Section 4 we compare the covering fraction of the outskirts of SFGs with atomic-dominated DLA gas (4.1) and with molecular-dominated gas (4.2). We then discuss the results in Section 5; we compare the results to those of Rafelski et al. (2011) (5.1), examine the two different possible normalizations of the $z \sim 1$ column-density distribution function (5.2), compare the results to predictions from Krumholz (2013) in Section 5.3, compare the results to the

SFR efficiency of local H I gas in Section 5.4, compare to measurements from the double DLA technique in Section 5.5, and consider the effects of dust (5.6). We summarize and conclude in Section 6.

For consistency with past results, we continue to use the Salpeter initial mass function (IMF; Salpeter 1955) and the Kennicutt far-UV (FUV) SFR calibration (Kennicutt 1998a) throughout this paper. To convert to the Kroupa IMF (Kroupa & Weidner 2003), divide all SFRs by a factor of 1.59. We adopt the AB magnitude system and an $(\Omega_M, \Omega_\Lambda, h) = (0.3, 0.7, 0.7)$ cosmology.

2. DATA ANALYSIS

The Hubble UDF ($\alpha (J2000) = 03^{\rm h}32^{\rm m}39^{\rm s}$, $\delta (J2000) = -27°47'29.''1$) includes the most sensitive and high-resolution images of any part of the sky. We restrict ourselves to this field due to the extreme faintness of the expected emission from DLAs. Even with this exquisite sensitivity, the signal-to-noise ratio (S/N) in the outskirts of individual high-redshift SFGs is insufficient to directly measure the spatially extended star formation from atomic-dominated H I gas. We therefore create composite stacks for this measurement. In this section, we describe the bandpass selection for measuring SFRs in Section 2.1, sample selection in Section 2.2, creation of the composite stacks in Section 2.3, and extraction of the radial surface bright profiles to measure emission in the outskirts of SFGs in Section 2.4. We also consider possible contamination from Lyα in Section 2.5. We use a procedure similar to that used in Rafelski et al. (2011), where we successfully measured emission in the outskirts of galaxies at $z \sim 3$.

2.1. Star Formation Rates

We determine spatially extended star formation around high-redshift SFGs by measuring their rest-frame UV flux. The UV is a sensitive measure of the SFR since the UV photons are produced by short-lived massive stars. We convert the measured flux to an SFR by the calibration from Kennicutt (1998a). We use three of the original ACS optical bandpasses, B, V, and i' (F435W, F606W, and F775W), corresponding to the rest-frame FUV and near-UV (NUV) fluxes. Only the rest-frame FUV data near 1500 Å were considered by Rafelski et al. (2011), and this light falls in the B and V bands at $z \sim 2$ and $z \sim 3$. However, the UV spectrum is nearly flat from 1500 to 2800 Å (Kennicutt 1998a), which allows measurements of the SFR from two independent bandpasses at $z \sim 2$ and $z \sim 3$ (V and i' bands), and it enables measurement of the $z \sim 1$ sample in the optical B band. While we do have images at 1500 Å for the $z \sim 1$ bin, the wavelengths fall in the WFC3/UVIS bandpasses. The UV images are less sensitive than the optical UDF images and potentially suffer from charge transfer inefficiencies (Teplitz et al. 2013; Rafelski et al. 2015).

The FUV and NUV SFR calibrations by Kennicutt & Evans (2012) are very similar, which further supports using the FUV and NUV images as independent SFR measurements, assuming a continuous star formation history (SFH). We test whether it is equivalent to measure the SFR from anywhere within the 1500–2800 Å window by examining the FUV–NUV color for the full sample[8] of SFGs in Figure 1. We find a median FUV–NUV color of 0.09 ± 0.16 mag at $z \sim 2$ and 0.04 ± 0.17 mag

_____
[8] See Section 2.2 for the definition of what the "full" sample is.
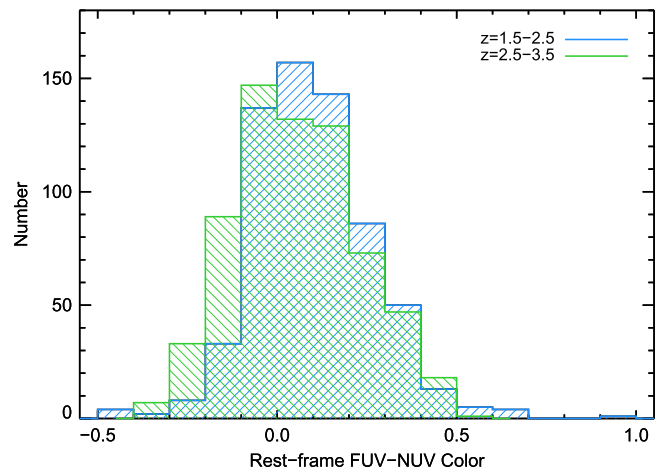
Figure 1. FUV–NUV rest-frame color for the full $z \sim 2$ and $z \sim 3$ samples. The median FUV–NUV color is close to 0, justifying the use of both the FUV and NUV images in measuring the SFR.

at $z \sim 3$, which suggests that either the FUV or the NUV flux will yield the same SFR for the majority of our sample. The width of the distribution is larger than our uncertainties, with a slightly positive spread. This may be due to dust extinction of our galaxies, since the FUV flux is lower than the NUV flux.

The rest-frame FUV light from normal high-redshift SFGs suffers from dust extinction by up to a factor of 5 (Reddy et al. 2012), which could reduce our measured SFR efficiency later in this paper. However, the dust is concentrated in the center of the galaxies in the highest star-forming region and is much reduced for lower-mass galaxies (Nelson et al. 2016). Similarly, Bigiel et al. (2010b) find that the FUV emission in the outskirts of local galaxies reflects the recently formed stars without large biases from external extinction. We similarly do not expect much extinction in the outer parts of SFGs, if it consists of atomic-dominated H I gas, as DLAs have low dust-to-gas ratios (Murphy & Liske 2004; Frank & Péroux 2010; Khare et al. 2012; Fukugita & Ménard 2015; Murphy & Bernet 2016). We therefore do not apply a dust correction to the SFRs, as the measured SFRs presumably occur in DLAs. However, we consider possible dust extinction further in Section 5.6.

We also note that the SFR calibrations are sensitive to metallicity, and decreasing the metallicity should increase the FUV luminosity for a given mass distribution, and thereby the SFR (Kennicutt & Evans 2012). Since DLAs have a metallicity of approximately 1/30 solar (Rafelski et al. 2012), the SFRs of DLA gas are potentially underestimated by ~ 0.1 dex. However, the change from this effect is small given that the evolution in metallicity from $z \sim 1$ to $z \sim 3$ is ~ 0.4 dex, and thus we do not consider it here.

2.2. Samples

We select galaxies using the photometric redshifts from Rafelski et al. (2015), which include the 11 *Hubble Space Telescope* (*HST*) bandpasses covering the UDF from the NUV to the near-IR (NIR; Beckwith et al. 2006; Oesch et al. 2010a, 2010c; Bouwens et al. 2011; Ellis et al. 2013; Illingworth et al. 2013; Koekemoer et al. 2013; Teplitz et al. 2013). The photometric redshift fits all cover either the Lyman break or the 4000 Å break of the galaxies, and most cover both breaks. This yields robust redshift estimates, as evidenced by comparisons

Table 1
Sample Properties

Sample	z_{min}	z_{max}	Full Samp	Sub Samp	Scale (kpc/″)	Volume (Mpc³)	DA (Mpc)
$z \sim 1$	0.7	1.5	802	36	8.01	24555	1652
$z \sim 2$	1.5	2.5	1329	30	8.37	36914	1727
$z \sim 3$	2.5	3.5	1178	43	7.70	37297	1589

Note. Redshift sample properties and adopted physical constants. Volume is the comoving volume sampled. DA is the angular diameter distance. The full sample is significantly larger than the subsample, which is due to a different magnitude cut, photometric redshift quality, and morphological selection.

to spectroscopic and grism redshifts (Rafelski et al. 2015). We emphasize that these redshift estimates are significantly better than those previously available, and this analysis would not be possible without the new NUV and NIR data.

In addition to the redshift selection, we require that the SED template from the photometric fit is an SFG, and since most galaxies at $z > 0.7$ are star-forming (Muzzin et al. 2013), this is a small reduction in sample size (8% at $z \sim 1$, down to 2% at $z \sim 3$). We also impose a $V < 29$ magnitude cut to help secure a sample with robust photometric redshifts, as the NUV images and the corresponding CANDELS (Grogin et al. 2011; Koekemoer et al. 2011) portions of the NIR images have 5σ depth of ~28–29 mag (Rafelski et al. 2015). We split our sample into three redshift bins, $z \sim 1$, $z \sim 2$, and $z \sim 3$, as described in Table 1. These redshift bins enable us to sample the rest-frame FUV light in the most sensitive optical bandpasses, and provide sufficient galaxies per bin for a robust stack. This set of selection criteria will be considered the "full" sample per redshift bin, while other selection criteria below will create the subsamples for stacking. We note that we do not put a requirement on the quality of the photometric redshift in this full sample, since its purpose is to provide the total number of galaxies at that redshift down to $V < 29$. This sample differs from the sample defined below, as it is meant to capture these galaxies down to a fainter magnitude than will be used for stacking. This is necessary for the completeness corrections discussed in Section 3.2.2, and we clarify which sample is used as necessary.

To create a composite stack of SFGs in each redshift bin, we select a sample with similar morphological and physical characteristics, and without nearby neighbors that can overlap the galaxies or cause dynamical disturbances. We therefore select compact, symmetric, and isolated galaxies in a similar fashion to Rafelski et al. (2011) and Hathi et al. (2008). Morphological parameters are determined with SExtractor (Bertin & Arnouts 1996) on the V-band image and selected using the FWHM for compactness and ellipticity $\epsilon = (1 - b/a)$ for circularity. We require an FWHM $\leqslant$ 2 kpc, $\epsilon \leqslant 0.25$, and no nearby objects brighter than 29th magnitude within 11 kpc. In addition, we visually inspect the galaxies and require that no nearby companion is visible, but would have just passed the magnitude cut. This enables us to maximize the sample size without any visible contaminants. We limit ourselves to galaxies with very good photometric redshift fits, with ODDS > 0.9 (Benítez 2000) and $\chi^2 < 4$, as this was found to produce reliable photometric redshift selected samples (Rafelski et al. 2009, 2015). Furthermore, we impose a $V < 28$ magnitude cut to ensure that the individual galaxies

have sufficient S/N in the optical images for morphological analysis, which also results in improved photometric redshifts for the stacked sample. These are basically the same criteria as by Rafelski et al. (2011), modified to be based on a physical distance for consistency between redshift bins. Table 1 lists the parameters for the various subsamples, including the scale used to convert to arcseconds. Thumbnails of the galaxies in each subsample to be stacked are shown in Figure 2.

The $z \sim 3$ redshift bin is the same as in Rafelski et al. (2011), but the improved photometric redshifts cause different galaxies to be selected. Of the 48 galaxies selected by Rafelski et al. (2011), 35 have new photometric redshifts in the range $2.5 < z < 3.5$. For the remaining 13 galaxies with different redshifts, 2 are catastrophically incorrect ($z < 1$), 5 include the redshift bin within their uncertainties, and the other 6 have a median redshift of $z \sim 2.3$. Although the Rafelski et al. (2011) study includes some galaxies with incorrect redshifts, the stacks are median values and thus are relatively robust against such systematics. Therefore, the results presented by Rafelski et al. (2011) are still valid. In Section 5.1 we find excellent agreement between our new results and Rafelski et al. (2011).

We compare the magnitude, color, and redshifts of the full sample and subsamples to check for any differences in the properties of the two samples. The magnitudes are measured in the F606W bandpass, the colors are based on the F435W–F160W, F435W–F850LP, and F105W–F160W colors, and the redshifts use the new photometric redshifts. Since the full sample and subsamples apply different magnitude cuts, we remove the additional magnitude cut for the subsample in this comparison, as we are interested in determining whether the morphological and redshift cuts result in any changes in the sample properties.

We find that the median values of magnitudes, colors, and redshifts are similar, with no systematic trends. We apply the Kolmogorov–Smirnov test and find that all three distributions are consistent with being drawn from the same parent population. The fact that the magnitudes are similar suggests that the SFRs of the two samples are similar. The similar distribution of colors suggests that the two samples are made up of the same stellar populations and have similar SFHs.

2.3. Composite Stacks

For each redshift sample, we create a galaxy stack by centering on each galaxy with a Gaussian fit to subpixel precision and shifting to a common reference grid with a damped sinc function, and then obtain the median of the images. This creates a stack that is insensitive to outliers, and therefore any single galaxy at an incorrect redshift, with an unidentified nearby neighbor, or with extreme Lyα emission would not significantly affect the stack. In Rafelski et al. (2011) we tested this stacking procedure and found it robust to varying brightness, color, or FWHM within a stack. We also tested the difference in taking the median and the mean, and although the central regions of the mean stacks where higher, we found little difference in the galaxy outskirts. Rafelski et al. (2011) therefore chose to use the median value rather than the mean, given that it is more robust to contamination or incorrect photometric redshifts, and we similarly use the median value here. We note that any minor potential biases from asymmetric star formation would be included in all the redshift bins and therefore not affect the evolution measurement.

Figure 2. Thumbnail images at $z \sim 1$ (left), $z \sim 2$ (middle), and $z \sim 3$ (right) of the subsample of galaxies used for stacking. The $z \sim 1$ and $z \sim 2$ thumbnails are from the F435W image, and the $z \sim 3$ sample is from the F606W image. This corresponds to the NUV at $z \sim 1$ and FUV at $z \sim 2$ and $z \sim 3$. The thumbnails are 2.4 ″ on a side, with F606W magnitudes and IDs from Rafelski et al. (2015) labeled on each thumbnail. We note that this is a larger region than is extracted below, and shows that the galaxies are isolated.

At $z \sim 2$ and $z \sim 3$ we include both the rest-frame FUV and NUV data within a single stack to improve the S/N, and thus stack in μJy rather than electrons due to the different zero points of the images. The $z \sim 2$ stack consists of the F435W and F606W images, and the $z \sim 3$ stack consists of the F606W and F775W images. For the $z \sim 2$ and $z \sim 3$ samples we also create stacks just in a single passband in the FUV and NUV and find them to have consistent radial surface brightness profiles. We choose to use the combined stacks to have the best S/N possible. The galaxy stacks are shown in Figure 3.

As a comparison sample, we also create stacks of stars in the same fashion based on the sample by Pirzkal et al. (2005). We only include stars that are not saturated in each passband, isolated from nearby galaxies, and with confirmed grism spectra. This leaves us with a sample of 12 stars. Since we wish

to determine the shape of the star's point-spread function (PSF) rather than the absolute normalization, and because the stars have a wider distribution of magnitudes, we scale each star by its peak in a two-dimensional Gaussian fit to improve the PSF determination. We do not scale the galaxy stacks since in those stacks the absolute measured flux value is important, and the galaxies have a smaller magnitude range. Also, for the $z \sim 2$ and $z \sim 3$ galaxy stacks, we create a combined PSF including stars in both bands.

2.4. Radial Surface Brightness Profiles

We extract radial surface brightness profiles from the three composite stacks in Figure 3 with the same methodology as by Rafelski et al. (2011). We use circular aperture rings with radial
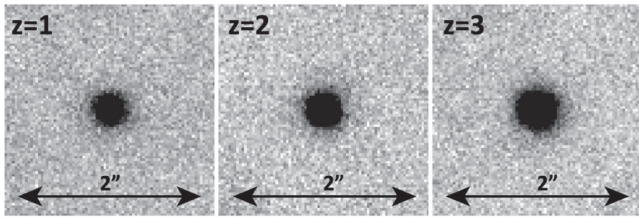
Figure 3. Images of galaxy stacks at $z \sim 1$, $z \sim 2$, and $z \sim 3$, each 2 ″ wide and stacked in μJy to avoid zero-point differences. The $z \sim 1$ stack includes the B band, the $z \sim 2$ stack includes B and V bands, and $z \sim 3$ stack includes V and i' bands.


widths of 1.5 pixels, with no overlap, providing independent measurements at each radius. The star stacks are extracted in the same way and then scaled to match the SFG stacks at the center. The extracted profile for each galaxy redshift bin and the relevant star profile is shown in Figure 4. The PSF declines more rapidly than the galaxy profile at all radii, which shows that the SFGs are resolved and have an extended profile.

The uncertainty on each ring is determined by the same bootstrap analysis described by Rafelski et al. (2011), with a sampling of 1000 iterations. In addition to the sky uncertainty added in quadrature, this includes the uncertainty in sample variance, which accounts for possible contamination in the sample, such as any catastrophic photometric redshift errors. The sky uncertainty is investigated by Rafelski et al. (2011), and we use the same procedure to obtain sky uncertainties here.

Specifically, we determine the local sky background for all the SFGs by measuring the sky background in each thumbnail using an iterative rejection routine to discard flux from outlying pixels. The background pixels are then fit by a Gaussian to obtain 1σ sky values, which also confirms that the sky level is at zero. The uncertainty in the sky decreases in the composite stack, and for a median stack in the Poisson limit it decreases by $1.25/\sqrt{N}$, where N is the number of images. This was confirmed for the UDF by Rafelski et al. (2011), and we therefore apply this to the 1σ sky values to obtain the stacked limits.

We further test the stacks by stacking empty regions of the sky and extracting their flux in the same fashion, and we find that the resulting flux levels are at or below this 1σ level, shown as the dotted line in Figure 4, confirming no leftover residual flux from the sky. The 1σ levels are different in the different panels in Figure 4 as they are determined in images at different wavelengths with different sensitivities.

The radial surface brightness depends on the sample selection described in Section 2.2. Since the magnitudes, colors, and redshifts of the subsample and full sample are similar, we conclude there that the two samples have the same stellar populations and have similar SFHs. Even so, the surface brightness profile is different if we stack the full sample or the subsample. This is investigated in Appendix B in Rafelski et al. (2011), and the result is that the full sample stack results in a surface brightness profile with a slightly elevated tail at larger radii. However, as noted in Rafelski et al. (2011), it is difficult to ascertain the amount of this emission that is caused by contamination from nearby neighbors or from morphologically different galaxies. If we ignore the contamination (which is significant), the SFR efficiencies determined in Section 3.2.3 would be increased by a factor of about two. This sets an upper limit on the any potential biases in sample selection on the radial surface brightness and the resultant SFR efficiencies.
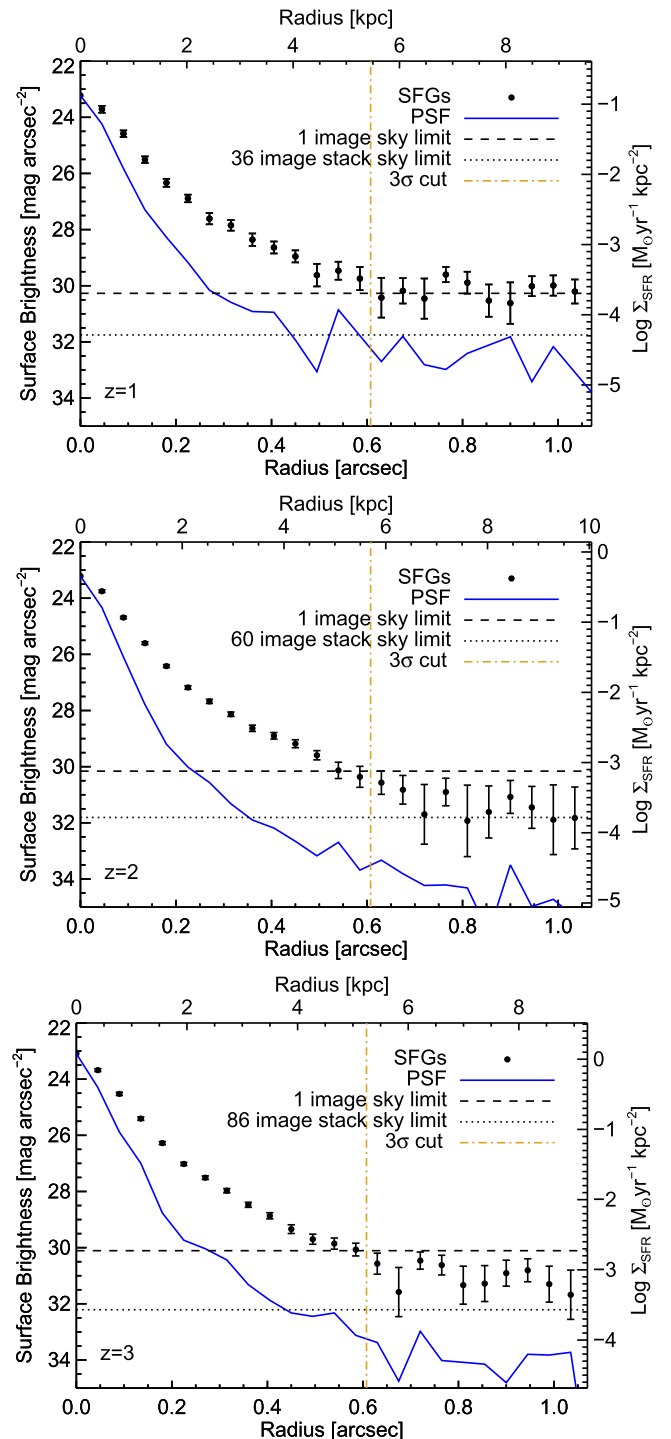
Figure 4. Radial surface brightness profiles for the three composite stacks at $z \sim 1$, $z \sim 2$, and $z \sim 3$ from Figure 3. These profiles show extended star formation in the outskirts of SFGs at high redshift and are used in determining the SFR efficiencies below. The black points are the SFG profiles, and the blue line is the PSF measured from stars. The dashed line is the 1σ sky uncertainty for a single galaxy, and the dotted line is the 1σ sky uncertainty for the stacked samples. Stacks of empty regions are at or below this dotted line. The uncertainties in the black points are a combination of the bootstrap uncertainty and the sky uncertainty. The gold dot-dashed line corresponds to the 3σ cut used in Section 3.2.2.

2.5. Effects of Lyα on the Surface Brightness Profiles

The Lyα emission line falls into the rest-frame FUV bandpass and could potentially contaminate the measured flux.

We consider whether Lyα could be contaminating our stacks, and thereby the resulting surface brightness profiles. Previously, Rafelski et al. (2011) conducted a test to see whether a typical SFG Lyα line would significantly affect the measured photometry by using the stacked LBG spectrum from Shapley et al. (2003) to estimate the effect, and found it to be negligible. However, it is possible that a subset of our sample has much stronger Lyα emission than a typical LBG, such as the green peas (Henry et al. 2015), which could bias the SFRs obtained from the rest-frame FUV continuum high.

To test for this possibility, in particular in the galaxy outskirts, we conduct the following tests. First, for the $z \sim 2$ and $z \sim 3$ samples we create a smaller sample including about half of the galaxies for which Lyα does not fall in the FUV bandpass by constraining the redshift, and compare the radial surface brightness profile of that stack to the full subsample stacks. We find no evidence of a decrease in the flux in the outskirts of the galaxies within their uncertainties. Second, we compare the radial surface brightness profiles for the FUV and NUV bands, since the NUV bands will not include the Lyα line. Again, we find no evidence of a change in the radial surface brightness profile in the outskirts.

The fact that the galaxies have the same radial surface brightness profile shapes in both bands suggests that the Lyα line has little to no effect on the radial surface brightness profiles. We note that this is not in conflict with the results by Steidel et al. (2011), who find extended Lyα halos around SFGs. First, that study samples a different galaxy population of brighter SFGs. Second, the Steidel et al. (2011) study goes out to ~80 kpc using ground-based observations, while we limit ourselves to the central ~10 kpc, which is barely resolved in that ground-based study. Third, Steidel et al. (2011) use narrowband filters to find the Lyα, while our stacks are in very broad filters, and thus the Lyα would not contribute except in the extreme emitter cases, and then only in the FUV bands for part of the redshift range.

3. SFR EFFICIENCY

The radial surface brightness profiles of the SFGs show spatially extended star formation in the galaxy outskirts. Star formation is expected in the outskirts of high-redshift galaxies, as it is measured in atomic-dominated hydrogen gas at low redshift (Thilker et al. 2007; Boissier et al. 2008; Fumagalli & Gavazzi 2008; Bigiel et al. 2010a, 2010b; Elmegreen & Hunter 2015). Such emission was also previously found at $z \sim 3$ by Rafelski et al. (2011) and interpreted as in situ star formation in atomic-dominated hydrogen at high redshift. In this paper we will work under the hypothesis that the observed emission in the SFG outskirts is from in situ star formation in atomic-dominated gas. We later consider this hypothesis in Section 4 by investigating the covering fraction of both atomic and molecular hydrogen gas compared to the observed emission.

In this section we aim to measure the evolution in the SFR efficiency from $z \sim 1$ to $z \sim 3$ using the radial surface brightness profiles of the SFGs. In Section 3.1 we determine the evolution in the normalization of the column-density distribution function of atomic-dominated neutral H I gas, $f(N_{H\,I})$, and in Section 3.2 we determine the efficiency. In Section 3.3 we transfer the results to a KS relation plot to visualize the efficiency and compare with other studies and models in Section 5.

3.1. Column-density Distribution Function

The SFR efficiency and covering fraction of the atomic-dominated neutral H I gas (DLAs) directly depend on $f(N_{H\,I})$. The $f(N_{H\,I})$ is generally modeled with a double power law to the number of high-density absorbers to background quasars in surveys such as the Sloan Digital Sky Survey (e.g., Ahn et al. 2012). It takes the form

$$f(N_{H\,I}, X) = k_3 \left(\frac{N}{N_d}\right)^\alpha, \quad \alpha = \begin{cases} \alpha_3; & N \leqslant N_d, \\ \alpha_4; & N > N_d, \end{cases} \quad (1)$$

where k_3 represents the normalization, α the slope, and N_d[9] the break column density ($N_{H\,I}$) in the double power law. The exact values of these vary depending on the analysis technique, redshift range, and survey (Prochaska et al. 2005; Noterdaeme et al. 2009, 2012; Prochaska & Wolfe 2009). The slope of $f(N_{H\,I})$ is not observed to evolve with time at any column density, but the normalization of $f(N_{H\,I})$ does show evolution (Prochaska & Wolfe 2009; Sánchez-Ramírez et al. 2016).

For consistency with Rafelski et al. (2011), we adopt $\alpha_3 = -2.0$ for $N \leqslant N_d$ (Prochaska & Wolfe 2009) and $\alpha_4 = -3.0$ for $N > N_d$. The value of α_4 is less certain than α_3, and the value used is consistent both with the formulation of randomly oriented disks used below and with the value measured by Noterdaeme et al. (2009).

With the value of the slopes set, we determine the other parameter values by fitting the data presented by Noterdaeme et al. (2012), including their completeness and systematic corrections.[10] First, we fit all the data simultaneously over the entire redshift range with log $N_{H\,I} > 20.3$, holding the slopes constant at the above values, and find log $N_d = 21.51$. We note that if we allow all parameters to be free, then we recover similar slope values as defined above.

We then fix both the slopes and N_d and split the data into four redshift bins. We use the same redshift bins as by Noterdaeme et al. (2012), except we combine the two highest-redshift bins to obtain better statistics. The resultant fits in Figure 5 show an evolution in the normalization k_3 with redshift. We find that log $k_3 = -23.86$, -23.94, -23.82, and -23.70 for the redshift bins $2.0 < z < 2.3$, $2.3 < z < 2.6$, $2.6 < z < 2.9$, and $2.9 < z < 3.5$, respectively. We investigate the evolution of the normalization in Figure 6, which shows a clear increase in the normalization of $f(N_{H\,I})$ with redshift. This is consistent with the redshift evolution observed in the integral quantities (incident rate and mass density) of DLAs (Noterdaeme et al. 2012). We note that while the DR12 sample of DLAs is not yet publicly available, the internal DR11 sample appears to be in good agreement in the high-$N_{H\,I}$ regime (Noterdaeme et al. 2014).

In addition to the redshift range directly sampled, we also require the value of the normalization at $z \sim 1$. However, due to the atmospheric cutoff, it is difficult to observe DLAs at $z < 2$, as it requires using space telescopes such as *HST*. Even if including all data obtained with *HST*, the resultant measure of the normalization of $f(N_{H\,I})$ at $z = 0.6$ has very large uncertainties (Neeleman et al. 2016, blue triangle). We therefore must obtain k_3 at $z \sim 1$ using a fit dominated by the high-redshift points, or with an interpolation including the

---

[9] Throughout this paper, all column densities are in log 10 with units of cm⁻².

[10] Noterdaeme et al. (2012) do not explicitly measure $f(N_{H\,I})$ as a function of redshift, just the cosmological mass density, which is the integrated quantity.
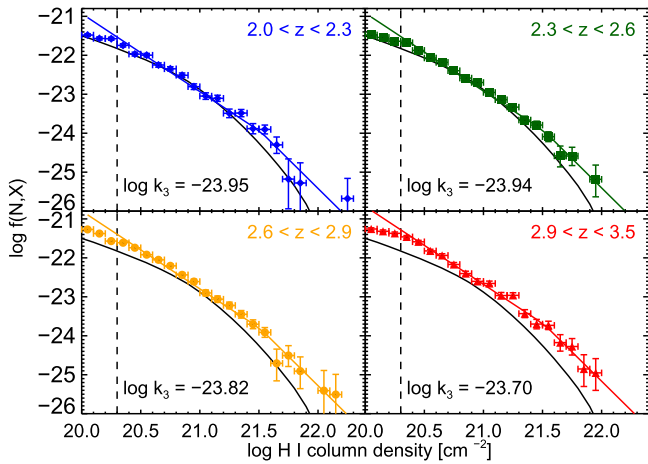
Figure 5. Fits to the column-density distribution function $f(N_{\rm H\,I})$ based on the data and corrections by Noterdaeme et al. (2012) in four redshift bins: $2.0 < z < 2.3$, $2.3 < z < 2.6$, $2.6 < z < 2.9$, and $2.9 < z < 3.5$ in blue, green, orange, and red, respectively. The data are shown as diamonds, squares, circles, and triangles, respectively, and the fits as the solid lines in their respective colors. The fits are only for $N \geqslant 20.3$, shown as a vertical dashed black line. We overplot the $z = 0$ value of $f(N_{\rm H\,I})$ as determined from 21 cm emission studies (Zwaan et al. 2005) for comparison, useful to visualize the evolution in the normalization of $f(N_{\rm H\,I})$ in each redshift bin. A clear increase in the normalization of $f(N_{\rm H\,I})$ with redshift is observed relative to the $z = 0$ value.
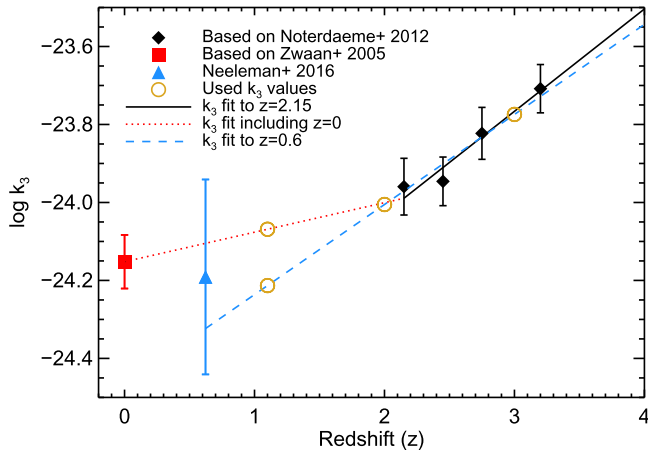
Figure 6. Evolution in the normalization of $f(N_{\rm H\,I})$, k_3, as a function of redshift. The gold circles mark the adopted values of k_3 used throughout this paper. The filled black diamonds are from the fits in Figure 5, and the black line is the best fit to these points. The red dashed line is obtained by connecting the $z = 0$ value with the $z = 2$ value. The blue triangle is from Neeleman et al. (2016), and the blue dashed line is a fit including the black diamonds and the blue triangle.

$z = 0$ value. The blue dashed line in Figure 6 is a fit to the log k_3 values at $z > 0.6$, and the black line is a fit to only the $z > 2$ log k_3 values. We adopt the resultant k_3 values from the blue dashed line, but note that an extrapolation of the $z > 2$ fit to $z \sim 1$ only differs from the full fit by 0.05 dex, due to the large uncertainties of the $z = 0.6$ point.

The shape of $f(N_{\rm H\,I})$ at $z = 0$ is different from the high-redshift ones, shown as the solid black line in Figure 5 based on Zwaan et al. (2005). This is likely due to the different method used to measure the H I gas, namely, 21 cm line emission rather than Lyα in absorption to background QSOs. Moreover, the exact shape and normalization of the $z = 0$ point are uncertain, with them depending on the data set and method used to obtain

$f(N_{\rm H\,I})$ (Braun 2012). For instance, Braun (2012) includes corrections at high column densities, which significantly changes the slope. Therefore, while we can fit the same function to the $z = 0$ data, it results in a poor fit due to the different (but uncertain) shape. However, the value of this fit is still useful to constrain possibilities for the value of k_3 at $z = 1$, and we therefore show it as the red square in Figure 6, and connect it to the $z \sim 2$ value with the red dotted line. This yields a second value for $z = 1$ by interpolating in between. We thereby have two possible values of k_3 at $z = 1$, and we consider both cases in what follows. We note that the first value of k_3 is consistent with a near-constant evolution between $z \sim 2$ and $z \sim 1$, whereas the second case is consistent with little to no evolution, and therefore the true k_3 value at $z \sim 1$ is likely bracketed by these two measurements. Figure 6 shows the four values of k_3 adopted in this paper as gold open circles.

3.2. SFR Efficiency Determination

We determine the SFR efficiency of atomic-dominated neutral hydrogen gas at each redshift by comparing the emission observed in the outskirts of SFGs in Figure 4 to the emission expected from DLAs based on a model that predicts the SFR density per intensity interval around the SFGs. This model and the framework to connect the observations to the model are described in detail in Section 6 of Rafelski et al. (2011).

The model adopts a disk-like geometry, the observed $f(N_{\rm H\,I})$, and the KS relation for different possible SFR efficiencies. The KS relation connects the SFR per unit area ($\Sigma_{\rm SFR}$) with the gas surface density ($\Sigma_{\rm gas}$), with parameters calibrated with observations of nearby disk galaxies (Schmidt 1959; Kennicutt 1998b). The KS relation is defined as

$$\Sigma_{\rm SFR} = K \times \left(\frac{\Sigma_{\rm gas}}{\Sigma_{\rm c}} \right)^{\beta}, \qquad (2)$$

where $\Sigma_{\rm gas}$ is the mass surface density perpendicular to the plane of the disk, $\Sigma_{\rm c} = 1\,M_{\odot}\,{\rm pc}^{-2}$, $K = K_{\rm Kenn} = (2.5 \pm 0.5) \times 10^{-4}\,M_{\odot}\,{\rm yr}^{-1}\,{\rm kpc}^{-2}$, and $\beta = 1.4 \pm 0.15$ (Kennicutt 1998b). We define the SFR efficiency as the percentage change in the normalization K in the KS relation. A 10% SFR efficiency would correspond to a model that reduces the normalization in the relation by a factor of 10, e.g., $K = 2.5 \times 10^{-5}\,M_{\odot}\,{\rm yr}^{-1}\,{\rm kpc}^{-2}$. We note that this is a different definition than what is often referred to as the star formation efficiency (e.g., Bigiel et al. 2010b), although the two are directly related.

In the next two subsections we guide the reader through the basic process to determine the SFR efficiency, but refer to Rafelski et al. (2011) for details, mathematical derivations, and equations. We describe the model in Section 3.2.1, describe the measurements and completeness corrections in Section 3.2.2, and compare the measurement and model to obtain the SFR efficiency in Section 3.2.3.

3.2.1. Model for DLA Emission

The model by Rafelski et al. (2011) is based on the model by Wolfe & Chen (2006), and predicts the expected UV emission from DLAs by multiplying the expected SFR per area for each column density of gas from the KS relation (Kennicutt 1998b)

with the area of the sky covered by that gas from the column-density distribution function of H I gas (e.g., Prochaska & Wolfe 2009). The model assumes that SFGs are at the center of DLAs, and that the in situ star formation in DLAs occurs in gaseous disks inclined on the plane of the sky, averaged over all possible inclination angles. Each differential interval of the SFR density represents a ring around the SFGs corresponding to a surface brightness and a solid angle interval subtended by each ring. It allows for a large range in disk thicknesses, covering both very thick and thin disks (aspect ratios R/H from 10 to 100). The model is dependent on redshift by $(1 + z)^3$ due to cosmological dimming and the K-correction, and also depends on the redshift evolution of k_3 in $f(N_{H I})$ shown in Figure 6.

The geometry of the model assumes that the gas column density of the disk (denoted as $g(N_\perp, X)$ in Rafelski et al. [2011] and defined in Equations (15) and (16) therein) decreases as a function of increasing radius and directly depends on $f(N_{H I}, X)$. The $g(N_\perp, X)$ also depends on the column density perpendicular to the disk, $N_\perp$, but since we integrate over all possible inclination angles, we do not need to know that quantity directly. By defining $f(N_{H I}, X)$ as a function of $g(N_\perp, X)$ in this model, we implicitly assert that all the DLA gas is within a gaseous configuration with a preferred plane of symmetry and a decreasing column density as a function of radius, such as a disk. This results in a distribution of gas column densities that reproduce $f(N_{H I}, X)$, but with the gas in a disk-like structure described by $g(N_\perp, X)$. We also consider the case where only half of the gas resides in such a disk (or only half contributes to the in situ star formation) in Section 7.4 of Rafelski et al. (2011) and also address it in Section 5.3 below.

We can predict the SFR density of the DLA gas as a function of the column density by applying the KS relation and integrating $g(N_\perp, X)$ over all possible inclination angles of the disk. The comoving SFR density, $\dot{\rho}_*$, with observed column density greater than N, is derived in Wolfe & Chen (2006) and shown there as Equation (6). This quantity is then modified in Rafelski et al. (2011) to be a differential expression with respect to the the column density to model the change in $\dot{\rho}_*$ as a function of the column density ($\frac{d\dot{\rho}_*}{dN}$, Equation (19) in Rafelski et al. 2011) and therefore also the radius of the disk. In order to compare this quantity with observations, we replace the column density by the observed intensity averaged over all inclination angles. The model thereby predicts the surface brightness (obtained from the KS relation) as a function of the differential comoving SFR density per observed intensity interval, $d\dot{\rho}_*/d\langle I_{\nu_0}^{\rm obs}\rangle$ (Equation (25) in Rafelski et al. 2011).

While this may seem to be a strange quantity, it enables a comparison of the model to the measured radial surface brightness profile, providing unique non-overlapping predictions for possible SFR efficiencies. The SFR efficiency is modified in the model by varying the normalization of the KS relation. For the model prediction, we directly use Equation (25) by Rafelski et al. (2011), along with the equations and constants it depends on therein. The only difference is that we modify the constants in $f(N_{H I})$, adopting the k_3 values for each redshift bin as described in Section 3.1.

The resulting predictions for the surface brightness versus $d\dot{\rho}_*/d\langle I_{\nu_0}^{\rm obs}\rangle$ for each redshift window are shown in Figure 7, where the blue line represents 100% SFR efficiency and the red lines correspond to reduced efficiencies as labeled in the figure.

A 10% SFR efficiency is obtained by reducing the normalization constant K by a factor of 10, where 100% efficiency corresponds to $K_{\rm Kenn} = (2.5 \pm 0.5) \times 10^{-4} M_\odot$ yr^{-1} kpc^{-2} (Kennicutt 1998b). Since there are two possible values of k_3 found at $z \sim 1$, we show the $z \sim 1$ results for two different k_3 values.

3.2.2. Measurement and Completeness Correction

In order to obtain an SFR efficiency below, we need to compare the model to the observations, which requires putting the observations into the same form as the model. Specifically, the radial surface brightness profiles from Figure 4 showing emission observed in the outskirts of SFGs need to be transformed onto the same surface brightness versus $d\dot{\rho}_*/d\langle I_{\nu_0}^{\rm obs}\rangle$ scale as the model. For each ring around the stacked SFGs, corresponding to a point in the radial surface brightness profile, we obtain a surface brightness and covering area and use it to determine $\Delta\dot{\rho}_*$ with Equation (28) by Rafelski et al. (2011). This equation depends on the number of SFGs in each redshift bin (from the full sample), the angular diameter distance, and the comoving volume sampled, which are all provided in Table 1. It also depends on the aspect ratio of the disk, which is an unknown quantity, but is likely contained in the range between 10 and 100, and therefore the resultant measurements of $\Delta\dot{\rho}_*/\Delta\langle I_{\nu_0}^{\rm obs}\rangle$ have a range of possible values.

We obtain $\Delta\langle I_{\nu_0}^{\rm obs}\rangle$ by measuring the intensity change across each ring by taking the difference of the intensity on either side of each point and dividing by two. If $\Delta\langle I_{\nu_0}^{\rm obs}\rangle$ were negative, then we would increase the interval over which we measure $\Delta\langle I_{\nu_0}^{\rm obs}\rangle$, as this would be due to noise fluctuations. This mainly occurs at radii that are later excluded due to low S/N. The resultant determination of $\Delta\dot{\rho}_*/\Delta\langle I_{\nu_0}^{\rm obs}\rangle$ is therefore obtained from the combination of the surface brightness, covering area, and intensity decrease over each ring. The redshift dependence of $\Delta\dot{\rho}_*/\Delta\langle I_{\nu_0}^{\rm obs}\rangle$ includes the same cosmological dimming and K-correction assumed in the model, and also includes the redshift in the angular diameter distance and in the comoving volume provided in Table 1.

Before adding the observations to Figure 7, we have to consider the completeness of the observations. First, we applied a magnitude cut of $V < 29$ to the full sample to ensure robust photometric redshifts. However, galaxies fainter than this magnitude cut and galaxies below the detection threshold would presumably also be surrounded by DLA gas, and thus some of the star formation will be missed. The details of the completeness corrections are provided in Appendix A3 by Rafelski et al. (2011), and we outline the procedure here. We first determine the number of missed galaxies from extrapolations of the luminosity functions of SFGs for each redshift bin integrated out to $V \sim 33$, where most of the contribution comes from galaxies at $29 < V < 31$. We use the luminosity function from Oesch et al. (2010b) for $z \sim 1$, Alavi et al. (2014) for $z \sim 2$, and Reddy & Steidel (2009) for $z \sim 3$, applying K-corrections of 0.24, 0.17, and 0.15, respectively.

In this correction, we assume that the shape of the radial surface brightness profile does not change for the fainter galaxies, and then for each ring we consider the number of SFGs missed and the fraction of flux missed for these galaxies in half-magnitude bins by scaling the profile to the integrated flux of the missed galaxies. This yields the amount of
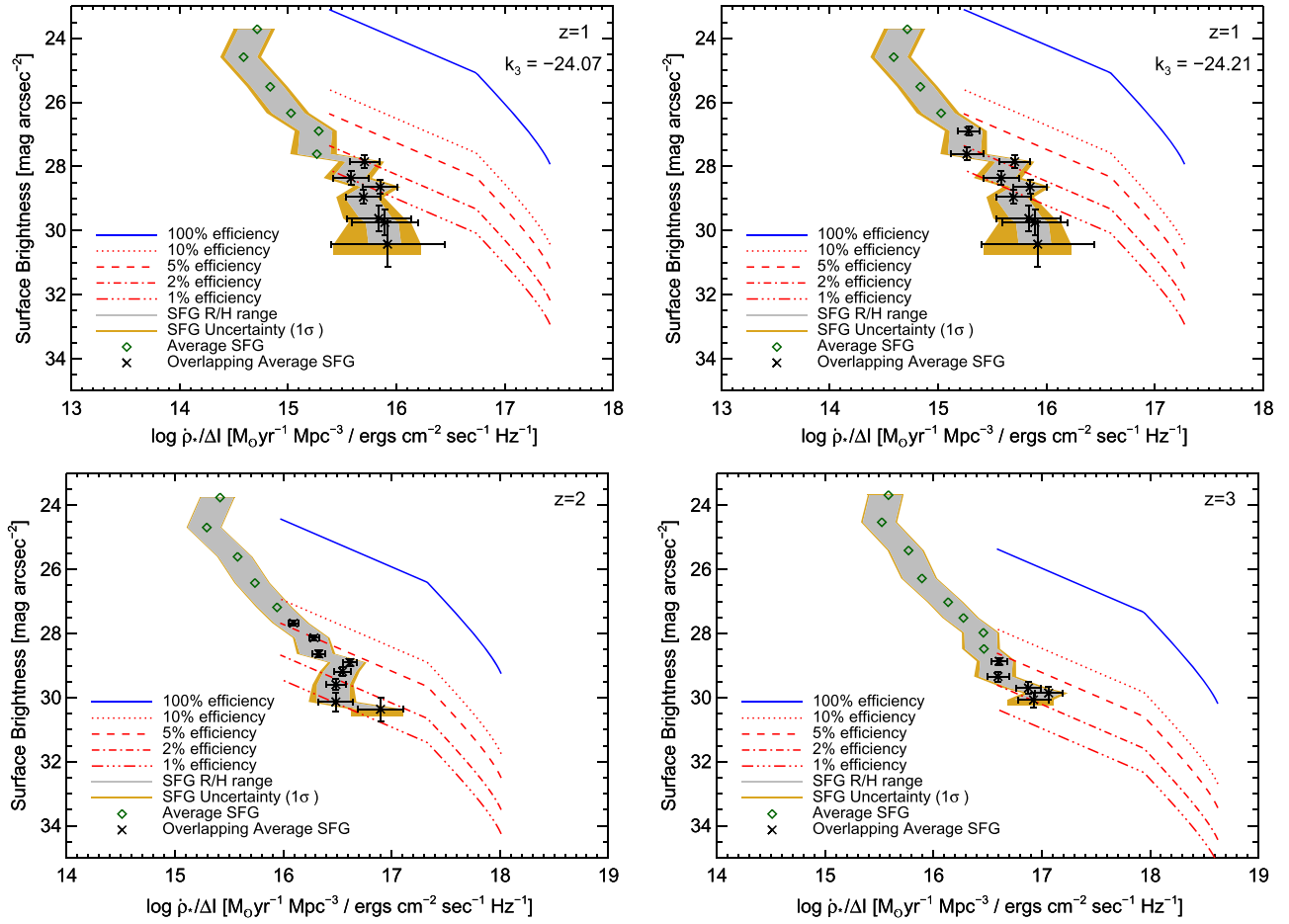
Figure 7. Surface brightness vs. the differential comoving SFR density per intensity ($\Delta\dot{\rho}_*/\Delta\langle I_{\nu_0}^{\mathrm{obs}}\rangle$), comparing the measured emission in the outskirts of SFGs to the predicted levels for atomic-dominated gas for different SFR efficiencies. Each panel corresponds to a redshift bin, and there are two $z \sim 1$ panels corresponding to the two possible values of k_3. The blue line represents the model at 100% efficiency, and the red dotted, short-dashed, dot-dashed, and triple-dot-dashed lines represent 10%, 5%, 2%, and 1% efficiency, respectively. The filled gray region represents the observed emission in the outskirts of SFGs for a range in aspect ratios, and the filled gold region is its 1σ uncertainty. The green diamonds are the average value of the possible aspect ratios, with the error bars including the uncertainty due to the variance in the composite stack. The SFR efficiency is obtained by comparing the measurements to the models, and the figures show SFR efficiencies of 1%–10%.

$\Delta\dot{\rho}_*/\Delta\langle I_{\nu_0}^{\mathrm{obs}}\rangle$ missed for each ring, which is added to the measurement of $\Delta\dot{\rho}_*/\Delta\langle I_{\nu_0}^{\mathrm{obs}}\rangle$. This results in an increase in $\Delta\dot{\rho}_*/\Delta\langle I_{\nu_0}^{\mathrm{obs}}\rangle$ by 60%–80% depending on the redshift, and the magnitude of the completeness correction can be visualized by comparing Figures 8 and 9 in Rafelski et al. (2011).

In Figure 7, we plot the completeness-corrected data using the same conventions as Rafelski et al. (2011), where the green diamonds and black crosses are for average values of the aspect ratio. The change of color and symbols marks the transition from UV emission that could be from atomic-dominated gas (black) to the inner regions of the SFGs that come from molecular-dominated gas (green), which is discussed further in Section 3.2.3. The error bars include the uncertainty in the aspect ratios, the variance due to stacking different SFGs obtained from the bootstrap method described above, and the measurement uncertainties. The gray shaded regions represent the range in aspect ratios, and the gold shaded regions the uncertainty on that range. We do not include possible systematic uncertainties in the FUV-to-SFR conversion factor, the column-density distribution function, or any such systematics. The data shown in Figure 7 are truncated at a maximum radius corresponding to a 3σ cut in Figure 4.

3.2.3. Comparison of Model and Measurement

With the differential $\dot{\rho}_*$ as a function of the radius from the central SFGs for both the model and the data, we can equate the two to determine an SFR efficiency. Doing so assumes that the FUV emission in the outskirts of the SFGs is on average emitted from the in situ star formation from atomic-dominated gas contained in a disk-like structure around these galaxies. As described in the introduction, the association of the DLAs with these SFGs is well established, and in addition this comparison assumes that the gas is in a disk-like geometry surrounding the SFGs. This assumption requires that the covering fraction of these disk-like structures around the SFGs approximately matches the covering fraction of the gas, which is checked in Section 4. In addition, there must be some point at which the molecular-dominated central star-forming cores transition to the atomic-dominated disk-like structure imposed by this comparison.

The transition from what is likely atomic-dominated to molecular-dominated gas in the data is determined by comparing the data and the model to each other and finding the value of $d\dot{\rho}_*/d\langle I_{\nu_0}^{\mathrm{obs}}\rangle$ in the model matching the measurement. We truncate the model at $N_{\mathrm{H\,I}} = 1.2 \times 10^{22}\,\mathrm{cm}^{-2}$, as above these column densities DLAs are not frequently

Table 2
Average SFR Efficiency

Redshift	log k_3	Efficiency
$z \sim 1$	-24.26	1.4 ± 1.0
$z \sim 1$	-24.07	0.8 ± 0.6
$z \sim 2$	-24.00	3.1 ± 1.7
$z \sim 3$	-23.77	2.8 ± 0.7

Note. Average SFR efficiency (based on the normalization of the KS relation; see Section 3.2) for different redshifts and log k_3. The uncertainty is the standard deviation of the various efficiencies measured for different surface brightnesses (and therefore $N_{\rm H\,I}$), and not the measurement uncertainty.

observed, likely due to the conversion from atomic to molecular hydrogen gas (Schaye 2001). This cut is marked by the left side of the red/blue model lines and by the color change in the data points from black to green. A small number of DLAs exist at higher column densities (Noterdaeme et al. 2014, 2015b), but this value is more typical and consistent with Rafelski et al. (2011).

The exact choice of the maximum $N_{\rm H\,I}$ does not affect the resultant SFR efficiencies, just the point at which we consider the gas to be transitioning from atomic-dominated gas to molecular-dominated gas, and therefore the transition from green to black points in Figure 7 (Krumholz et al. 2009a, 2009b). We acknowledge that there is likely a transition region where the gas is not fully in a single phase, and thus it is possible that our most luminous atomic-dominated point may not be from purely atomic-dominated star formation.

The models and the data do appear to have somewhat different slopes, which suggests that there may be a change in the efficiency of the gas as a function of the radius of the SFGs. This effect appears to be stronger in the lower-redshift data than that at $z \sim 3$, although the uncertainties on the data that suggest a different slope are also larger. While this change in efficiency as a function of radius may be real, we believe that the data are not sufficiently good to make accurate measurements of the slope, and therefore this effect. If real, it would suggest that the efficiency is decreasing as we go out in radius, but better data would be required to investigate the physical origin of this trend.

With the model and observations on the same plot, it is straightforward to obtain the SFR efficiency of each ring around the SFGs by comparing the model and the measurements in the atomic-dominated regime. For each measured point corresponding to a ring around the SFGs, we match it to the overlapping model (with a finer grid than plotted) and thereby obtain the SFR efficiency from that model. Overall, the SFR efficiency of neutral atomic-dominated hydrogen gas ranges from ~1% to 6% depending on the surface brightness (and therefore $N_{\rm H\,I}$), with mean values around 2% as shown in Table 2.

3.3. Visualizing the SFR Efficiency

At this point we have determined an SFR efficiency for each ring in the radial surface brightness profile, but this quantity is difficult to compare between redshifts and, more importantly, with other studies. As a tool to understand the low SFR efficiencies, to compare the efficiencies in different redshift bins to each other, and to compare the results to other studies,

we translate the results to a common set of quantities, namely, $\Sigma_{\rm SFR}$ and $\Sigma_{\rm gas}$. We emphasize that at this point the SFR efficiency is already measured and that this is purely a visualization tool. The details of this conversion are described in Section 6.3 in Rafelski et al. (2011), but we guide the reader through the process here.

The $\Sigma_{\rm SFR}$ can be directly obtained from the intensity of the emission in the outskirts of the SFGs as measured in the radial surface brightness profile by Equation (4) in Rafelski et al. (2011). This averages the SFGs over all disk inclination angles and applies the KS relation and the FUV-to-SFR conversion to obtain $\Sigma_{\rm SFR}$ directly from the intensity. The corresponding $\Sigma_{\rm gas}$ is indirectly obtained by taking $\Sigma_{\rm SFR}$ and plugging it into the the KS relation for the measured reduced SFR efficiency. We plot $\Sigma_{\rm SFR}$ versus $\Sigma_{\rm gas}$ for each redshift bin in Figure 8. We note that the corresponding column density for $\Sigma_{\rm gas}$ is obtained by unit conversion and the number of atoms per solar mass.

We make a more direct comparison of the SFR efficiencies as a function of redshift in Figure 9, showing the SFR efficiency as a function of $\Sigma_{\rm gas}$ for each redshift bin. The variation in the $z \sim 1$ points shows the importance of the value of k_3 from the column-density distribution function in determining the SFR efficiency. The blue points in the figure correspond to the linear fit of the k_3 values in Figure 6, while the red points correspond to the extrapolation to the poor $z \sim 0$ fit. The points show little evidence of evolution with redshift, except potentially the $z \sim 1$ red points, but see the discussion in Section 5.2. We emphasize that by construction our results average the data on the scale of a few hundred parsecs, and thus we measure an efficiency that is not purely the local one. In addition, the observations are only sensitive to the highest-column-density DLAs, resulting in measurements of $\Sigma_{\rm gas}$ at the high end of $f(N_{\rm H\,I})$. However, based on the radius at which we measure the emission, we expect to measure the highest-$N_{\rm H\,I}$ DLAs based on the correlation of $N_{\rm H\,I}$ with impact parameter $N_{\rm H\,I}$ (Péroux et al. 2016).

4. COVERING FRACTION

Throughout this paper we assume that the outskirts of SFGs form stars in situ out of neutral atomic-dominated hydrogen gas. In order for this assumption to hold, the area on the sky covered by the emission around SFGs must be similar to the area covered by this type of gas at that redshift. At the same time, we could ask the reverse question: whether or not the area on the sky covered by molecular-dominated gas can account for this emission. To address this, we compare the covering fraction of the emission to that of atomic-dominated gas in Section 4.1 and to molecular-dominated gas in Section 4.2, following the same methodology as described in Section 5.2 of Rafelski et al. (2011) and summarized here.

The cumulative covering fraction, C_A, is obtained by integrating the hydrogen column-density distribution function $f(N_{\rm H}, X)$ for gas columns greater than column density N up to a maximum column $N_{\rm max}$. This holds for both atomic and molecular hydrogen gas, with

$$C_A(N) = \int_{X_{\rm min}}^{X_{\rm max}} dX \int_{N}^{N_{\rm max}} dN_{\rm H} f(N_{\rm H}, X), \quad (3)$$

where X is the absorption distance. dX is defined as

$$dX \equiv \frac{H_0}{H(z)}(1 + z)^2 dz, \quad (4)$$
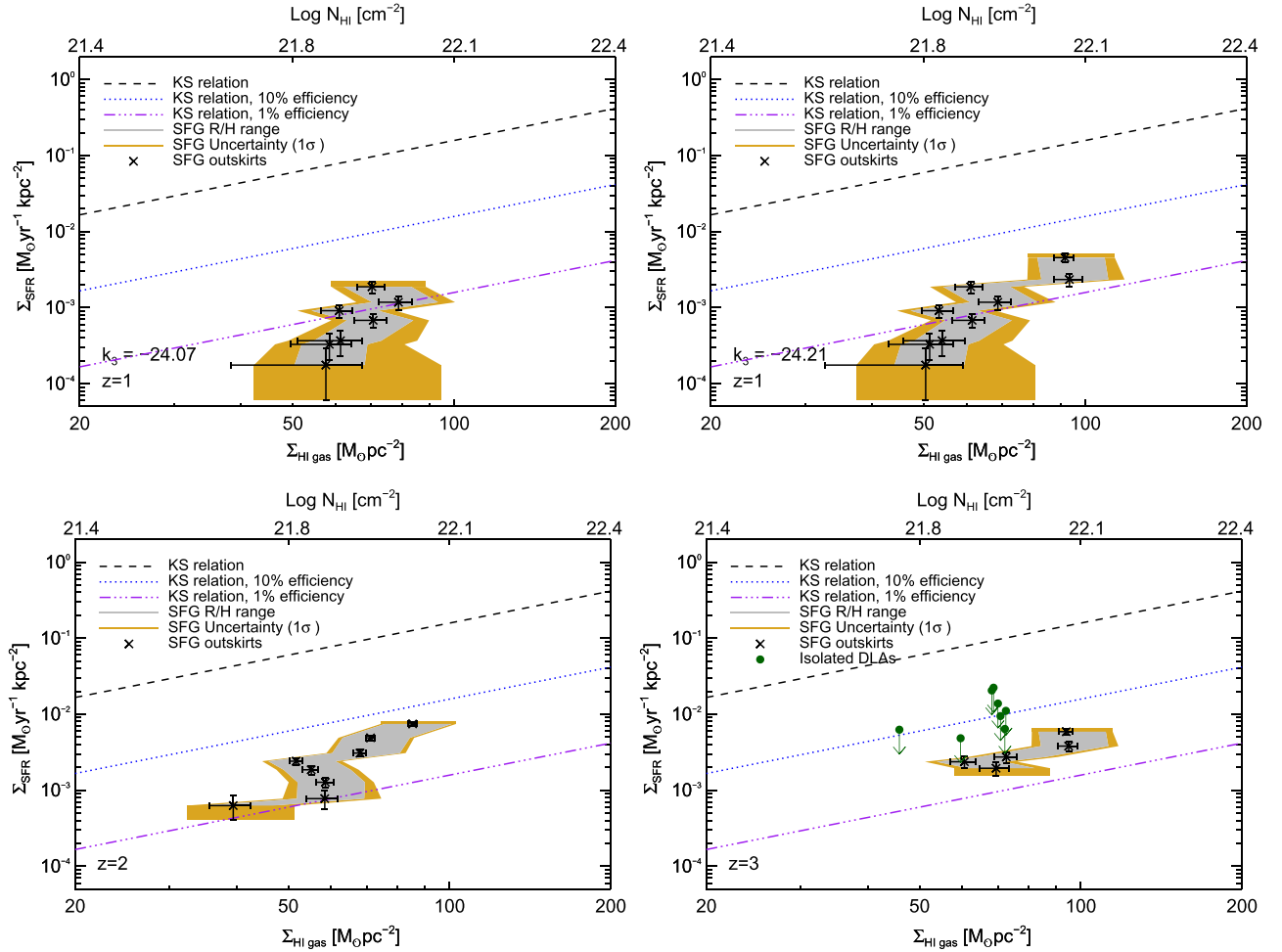
Figure 8. SFR per unit area (Σ_{SFR}) vs. gas density (Σ_{gas}) used to visualize the reduced SFR efficiency. Each panel corresponds to a redshift bin, and there are two $z \sim 1$ panels corresponding to the two possible values of k_3. The dashed black line represents the KS relation for 100% SFR efficiency, the dotted blue line is for 10% efficiency, and the dot-dashed purple line is for 1% efficiency. The gray filled region, the gold filled region, and the black crosses represent the same data as in Figure 7. The green data points in the $z \sim 3$ panel correspond to upper limits derived for DLAs without central bulges of star formation from Wolfe & Chen (2006) converted to work with this plot by Rafelski et al. (2011). The data all fall below 10% of the KS relation at all redshifts, showing a reduced SFR efficiency. However, no clear evolution with redshift in the SFR efficiency is observed between $z \sim 1$ and $z \sim 3$.

where $H(z)$ is the Hubble parameter at redshift z and H_0 is the Hubble constant. The column-density distribution function is different for atomic-dominated and molecular-dominated hydrogen gas, and we consider the covering fraction for each below.

4.1. Covering Fraction of Atomic-dominated Gas

We investigate whether the covering fraction of neutral atomic-dominated hydrogen gas (i.e., DLAs) is consistent with the covering fraction of the outskirts of SFGs. To do so, we integrate Equation (3) using the best-fit parameters for $f(N_{H\,I}, X)$ described in Section 3.1. Since we have two possible values of k_3 at $z \sim 1$, we have two covering fraction possibilities for that redshift. We use the same N_{max} of $N_{H\,I} = 1.2 \times 10^{22}\,cm^{-2}$ as in Section 3.2.3. We note that the observables used for the covering fraction comparison are the same as those used in the efficiency measurement, and therefore by construction this is not a completely independent measurement. However, this comparison is less model dependent than the efficiency measurement and is thus an important cross-check.

We compare the cumulative covering fraction of DLAs to that of the SFG outskirts as a function of surface brightness (and therefore column density) in Figure 10. The blue dotted line is the covering fraction for DLAs forming stars according to the KS relation at 100% efficiency, and the red dot-dashed, short-dashed, and triple-dot-dashed lines represent 10%, 5%, and 2% efficiency, respectively. The efficiency is again reduced by reducing the normalization of the KS relation. The black line is the covering fraction of the SFG outskirts, which is obtained by the total area covered by the radial surface brightness profile above that surface brightness times the number of SFGs in the full sample for that redshift bin, divided by the total area of $11.40\,arcmin^2$. Since this number depends on the number of observed galaxies, it requires a completeness correction for fainter objects not included in the full sample.

The completeness correction is obtained following Equation (A1) from Appendix A1 in Rafelski et al. (2011). We first determine the number of missed galaxies from the luminosity functions described in Section 3.2.2 for each redshift bin. For each half-magnitude bin of missed galaxies, we scale the radial surface brightness profile to that magnitude and determine the area that the outskirts of the scaled profile cover for each
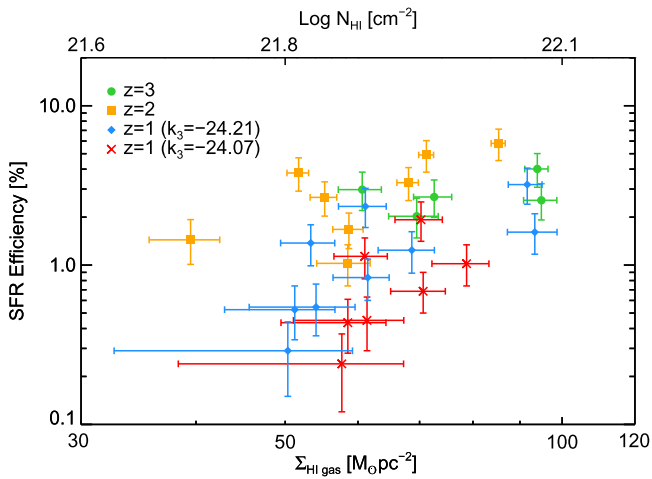
Figure 9. SFR efficiency vs. implied Σ_{gas} shown for different redshifts. The green circles correspond to the $z \sim 3$ SFGs, the orange squares to those at $z \sim 2$, and the blue diamonds and red crosses are for those at $z \sim 1$. The blue diamonds correspond to $\log k_3 = -24.26$, obtained by a fit to the $z > 2$ k_3 values. The red crosses are for $\log k_3 = -24.07$, obtained by an interpolation of the $z \sim 2$ point and the poor fit to the $z \sim 0$ data. All the data except the red $z \sim 1$ points show no evolution with redshift, while the red points may suggest a mild decrease at lower redshift. However, see the discussion in Section 5.

surface brightness. The missed covering fraction is the sum over the half-magnitude bins of the missed area times the missed number of galaxies. The resulting completeness-corrected covering fraction as a function of surface brightness is shown in gold in Figure 10. While the number of galaxies increases quickly with decreasing galaxy luminosity, the scaling of the outskirts of the radial surface brightness profile drops more rapidly, and thus only the bright end of the luminosity function contributes. We note that we only consider the outskirts of the SFGs, which leads to a different correction than would be needed for molecular gas in Section 4.2.

A comparison of the completeness-corrected covering fraction of the SFG outskirts and DLAs in Figure 10 reveals that the two agree at a somewhat higher SFR efficiency than expected (e.g., Figure 9). Specifically, the covering fractions agree for SFR efficiencies of $\sim 5\%$–20%, compared to the measured efficiencies of $\sim 1\%$–5%, resulting in differences by factors of ~ 3 in efficiency, or $\lesssim 5$ in covering fraction. This discrepancy in the SFR efficiency is not a large concern, as there are many assumptions that could cause systematic uncertainties on both the covering fraction and SFR efficiency. For instance, the covering fraction is directly dependent on the transition point from molecular-dominated to atomic-dominated gas, marked by the change from green to black points in Figure 7. The redshifts with higher covering fractions are also those that have this transition occur at smaller radii ($z \sim 2$ and $z \sim 1$ for $k_3 = -24.26$). We note that this uncertainty applies to the overall normalization and is not an uncertainty as a function of redshift.

It is possible to reduce the observed covering fraction by increasing the radius for the transition from atomic to molecular gas. Changing this transition point by ~ 1 kpc for the $z \sim 2$ data lowers the observed covering fraction such that it tracks the DLA covering fraction at a $\sim 5\%$ SFR efficiency. It is therefore possible that the transition point from molecular- to atomic-dominated gas may occur at a point further out than we assume in this paper, especially at $z \sim 1$ and $z \sim 2$. Given this possible systematic, the general agreement of the covering fraction and

SFR efficiency shows that there is sufficient DLA gas to account for the emission observed in the outskirts of high-redshift SFGs.

4.2. Covering Fraction of Molecular-dominated Gas

In this section we consider whether the emission observed in the outskirts of SFGs could come from molecular-dominated gas. Similar to Section 4.1, we calculate the covering fraction of molecular-dominated gas using Equation (3), which requires $f(N_H)$ for molecular-dominated gas ($f(N_{H_2})$). There currently are no measurements of $f(N_{H_2})$ at high redshift, so we use the low-redshift measurement and consider possible evolution. Since we do not have direct high-redshift measurements, this section is speculative, but the results presented in the remainder of the paper are not dependent on the analysis presented in this section.

We use the observed $f(N_{H_2})$ from Zwaan & Prochaska (2006), who determine a lognormal fit to the BIMA SONG sample (Helfer et al. 2003) defined as

$$f(N_{H_2}) = f^* \exp\left[\left(\frac{\log N - \mu}{\sigma}\right)^2 / 2\right], \quad (5)$$

where $\mu = 20.6$, $\sigma = 0.65$, and the normalization f^* equals $1.1 \times 10^{-25}\,\mathrm{cm}^2$ (Zwaan & Prochaska 2006). We adopt $N_{max} = 10^{24}$, which is the largest observed value of $f(N_{H_2})$. We use the KS relation with a normalization and slope for molecular gas from Bigiel et al. (2008), $K = K_{Biegel} = 8.7 \times 10^{-4}\,M_\odot\,\mathrm{yr}^{-1}\,\mathrm{kpc}^{-2}$, and $\beta = 1.0$. From this we can obtain the local covering fraction, which is shown as the purple short-dashed line in Figure 11. However, given the evolution of the mass density and the SFR density of the universe, the covering fraction likely evolves between $z = 0$ and $z \sim 3$, and we consider that possibility below.

The evolution of $f(N_{H_2})$ would be due to a change in either the slope or normalization, and here we consider only an evolution in the normalization for the following reasons. First, atomic-dominated gas only appears to evolve in normalization (e.g., Prochaska & Wolfe 2009). Second, we have no observational constraints for an evolution in the slope. We consider two possible methods to determine the evolution in the normalization. We use the evolution of the mass density of molecular gas (Ω_{H_2}) and the SFR density of galaxies.

The evolution of Ω_{H_2} is not well constrained by observations, but is carefully explored in models. Figure 5 in Walter et al. (2014) shows the evolution for a range of cosmological models and upper limits from CO observations in the Hubble Deep Field North (Obreschkow & Rawlings 2009; Lagos et al. 2011, 2014; Popping et al. 2014; Sargent et al. 2014). These results suggest an evolution of Ω_{H_2}, with an increase from $z = 0$ to $z = 3$ by a factor of ~ 5.

The evolution of the SFR density is better constrained by observations (Schiminovich et al. 2005; Reddy & Steidel 2009; Bouwens et al. 2015), and Figure 18 in Bouwens et al. (2015) shows a compilation of the evolution. This suggests an evolution of the SFR density from $z = 0$ to $z \sim 2$ of ~ 10. The SFR density turns over again at $z \gtrsim 2$, and hence the maximum evolution is a factor of ~ 10.

We therefore consider an evolution in the normalization (f^*) by a factor of 5 and 10, shown as pink triple-dot-dashed and cyan dot-dashed lines in Figure 11. In addition, there may be
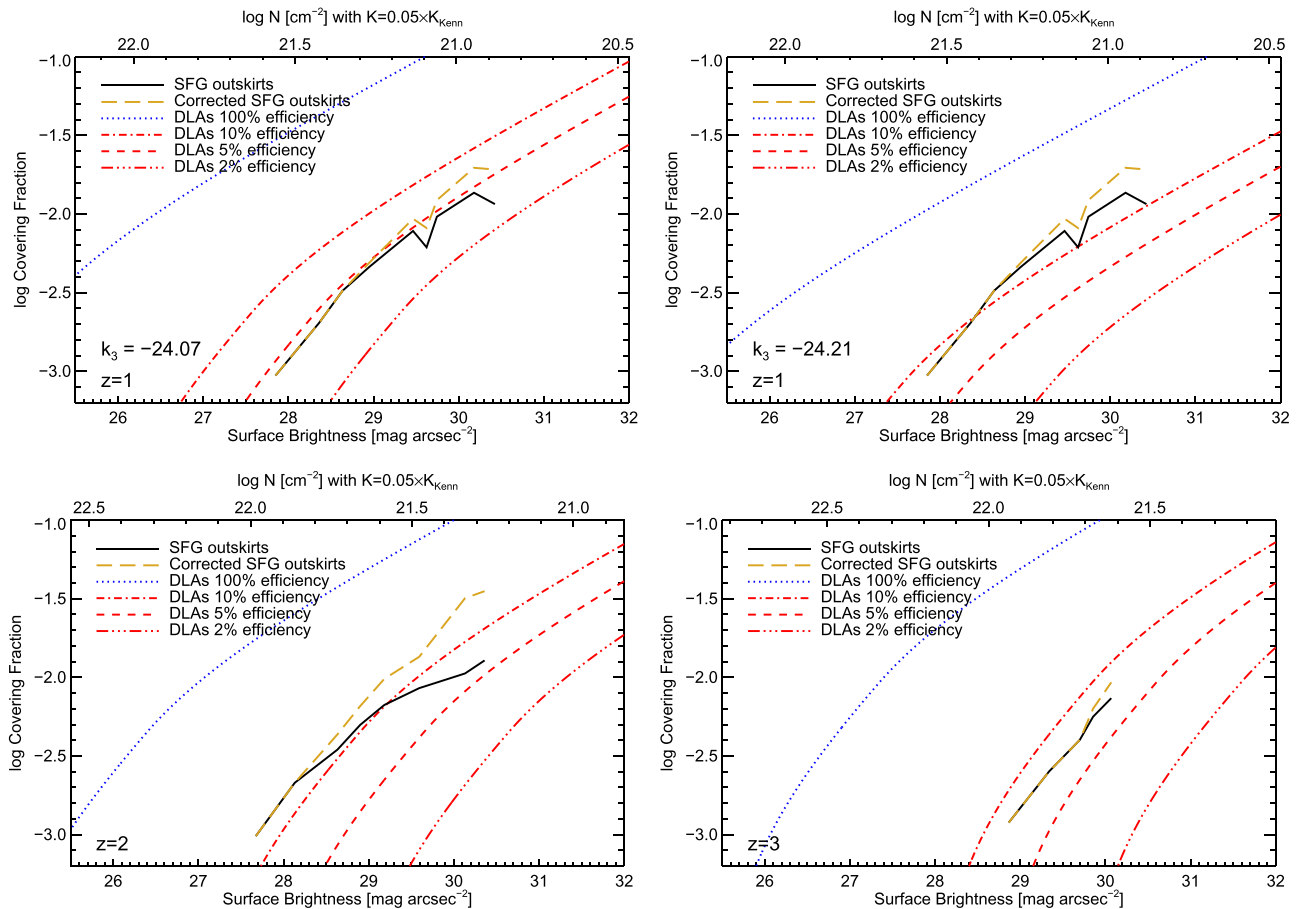
Figure 10. Cumulative covering fraction of DLAs as a function of surface brightness compared to the covering fraction of the outskirts of SFGs. The surface brightness depends on both the column density of the DLAs and the SFR efficiency. The black line is the covering fraction of the SFG outskirts, and the gold dashed line is the same corrected for completeness. The blue dotted line is the covering fraction for DLAs forming stars according to the KS relation at 100% efficiency, and the red dot-dashed, short-dashed, and triple-dot-dashed lines represent 10%, 5%, and 2% efficiency, respectively. The column densities labeled at the top of each panel are for a 5% efficiency, similar to the measurements. The general agreement of the covering fraction at similar SFR efficiencies shows that there is suficient DLA gas to account for the emission observed in the outskirts of SFGs.

molecular-dominated gas down to lower column densities than observed, and thus we extrapolate the data out to lower column densities with gray lines continuing each of the three $f(N_{H_2})$ lines. We compare these cumulative covering fractions to that of the SFGs (black lines) in Figure 11. The covering fraction of the SFGs is different from that shown in Figure 10, as it now includes both the outskirts and the inner cores of the galaxies. We note that if there is no molecular gas down to these densities, then the covering fraction of molecular gas would be truncated at some surface brightness <32 mag in Figure 11.

Similar to Section 4.1, a completeness correction is required, and we use the same procedure described there, except in this case we also include the inner cores of the SFGs in addition to the outskirts. The completeness-corrected molecular-dominated covering fraction is shown as the gold dashed line in Figure 11. This completeness correction is significantly larger than for the atomic-dominated case shown in Figure 10, because the cores of the SFGs are significantly brighter than the outskirts, and therefore the same faint galaxies contribute more at a given surface brightness. Since there is a significantly larger number of faint SFGs, and since their cores contribute to the covering fraction for a given surface brightness, this results in a larger overall covering fraction.

Comparing the covering fraction of SFGs to molecular-dominated gas in Figure 11 shows that there is insufficient

molecular-dominated gas for surface brightnesses $\gtrsim 28.5$ mag arcsec^{-2}, assuming a factor of 10 increase in f^* based on the evolution of the SFR density. If we instead use the factor of five evolution based on the evolution of Ω_{H_2}, then the covering fraction is insufficient for surface brightnesses $\gtrsim 27.5$ mag arcsec^{-2}. We emphasize that a factor of 10 increase in f^* is an upper limit to the evolution of f^*, as it assumes that all the evolution in the SFR density is due to an evolution in $f(N_{H_2})$.

We note that the molecular gas is traced indirectly via CO emission, yet the conversion factor between CO emission and H_2, X_{CO}, is metallicity dependent, increasing with decreasing metallicity (Wolfire et al. 2010; Bolatto et al. 2011, 2013; Elmegreen et al. 2013; Amorin et al. 2016). In addition, there may be a large component of "dark" molecular gas that is missed by tracing H_2 with CO observations. Specifically, in low-metallicity environments H_2 may be shielded, while the CO could be photodissociated (Wolfire et al. 2010). The fraction of this CO-dark gas is also metallicity dependent (Leroy et al. 2011), and it is not clear how much of the CO-dark gas exists at low metallicity (Langer et al. 2014). The result is that the molecular content of metal-poor gas is poorly constrained, adding significant uncertainty to the covering fraction of molecular gas, which is likely underestimated. As a
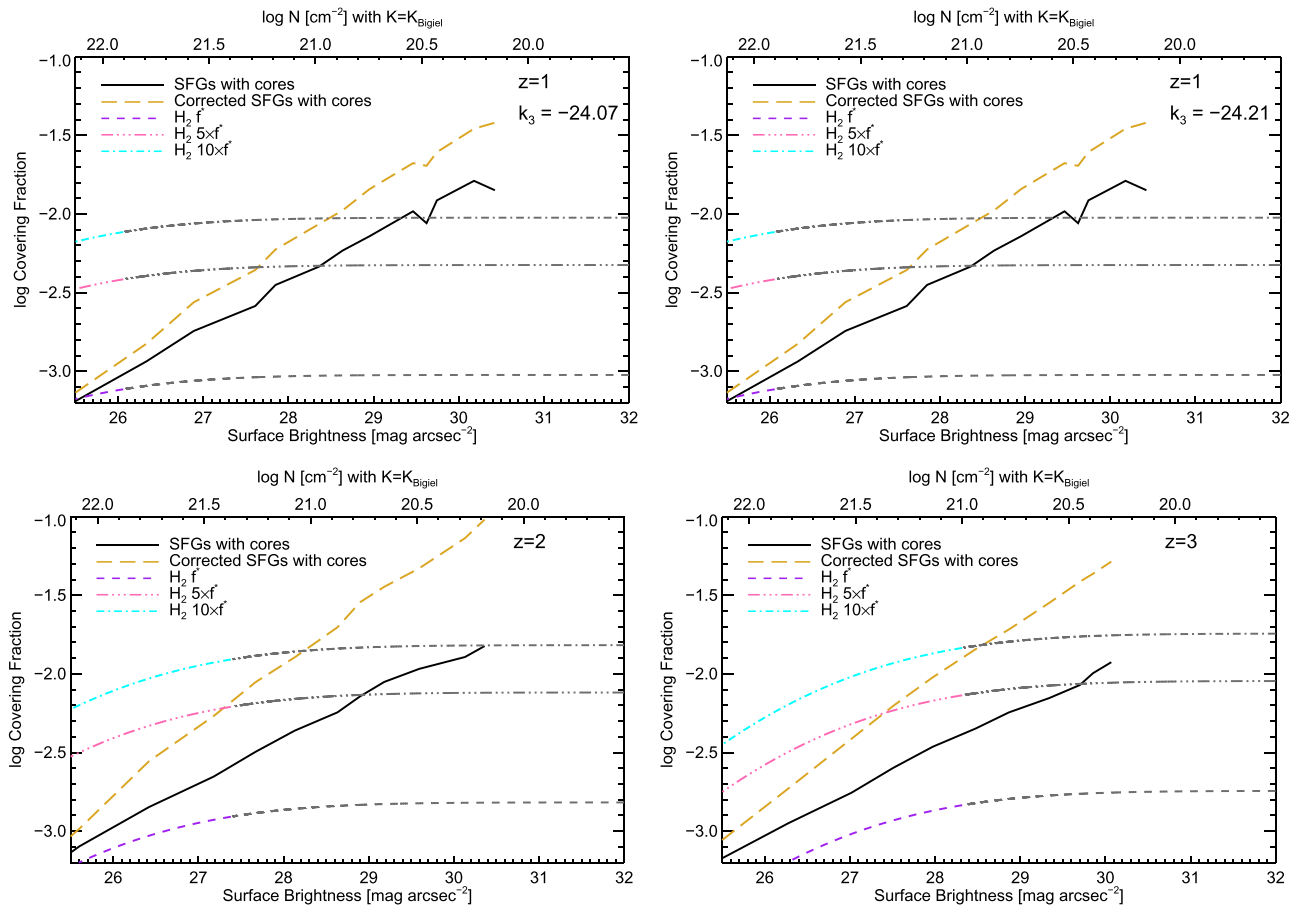
Figure 11. Cumulative covering fraction of molecular-dominated gas as a function of surface brightness compared to the covering fraction of SFGs. This figure is similar to Figure 10, but is for molecular-dominated rather than atomic-dominated gas. The black line is the covering fraction of the SFGs, and the gold dashed line is the same corrected for completeness. The purple short-dashed line is the covering fraction of molecular hydrogen with no evolution, the pink triple-dot-dashed line is the same with an evolution of five times f^* (the normalization of the column-density distribution function of molecular gas), and the cyan dot-dashed line is the same with an evolution of 10 times f^*. The gray lines continuing the purple, pink, and cyan lines are extrapolations of the data to lower column densities. The column densities labeled at the top of each panel are for $K = K_{\mathrm{Biegel}}$. The insufficient covering fraction of molecular-dominated gas at low surface brightnesses suggests that the outskirts of SFGs are unlikely to be from molecular-dominated gas.

consequence, the discussion presented in this section is speculative.

Combining the covering fraction results from atomic-dominated gas with those from the molecular-dominated gas shows that atomic-dominated gas can account for the observed emission at $\gtrsim 28$–29 mag arcsec^{-2}, while molecular-dominated gas does so at $\lesssim 27.5$–28.5 mag arcsec^{-2}. This suggests that there may be some overlap in the two, with a possible transition region where star formation occurs in both atomic-dominated and molecular-dominated gas. Regardless, it is unlikely that the outskirts of SFGs are forming stars out of molecular-dominated gas since not enough of the sky is covered by this gas to account for the observed emission. We note that while this is the case averaged over the H I disks, there could be embedded molecular regions within the disks. In fact, molecular hydrogen is sometimes observed in absorption systems (Noterdaeme et al. 2015a, 2015b), suggesting that this is indeed the case for at least some systems. Further observations of $f(N_{\mathrm{H_2}})$ at higher redshift and down to lower gas densities are needed to further this comparison, but it is not a critical part of this analysis.

Observations of molecular hydrogen in DLAs are very rare, with less than 6% of the DLA population showing the Lyman and Werner transitions (Jorgenson et al. 2014). However, when considering a somewhat biased sample of DLAs, there appears to be an increase in the fraction of DLAs with molecular hydrogen as a function of H I column density (Noterdaeme et al. 2015a). This is again consistent with the above picture of a transition region with star formation in both atomic-dominated and molecular-dominated gas, as this overlap region would occur at the highest H I column densities for DLAs.

5. DISCUSSION

Under the assumption that outskirts of SFGs are composed of atomic-dominated H I gas, the SFR efficiency of this gas is significantly reduced compared to the KS relation and shows little to no evolution with redshift (see Figure 9). This assumption is supported by the fact that the covering fraction of molecular-dominated gas is insufficient to explain the emission in the outskirts of SFGs, while the covering fraction of atomic-dominated gas roughly covers the emission. The reduced efficiency is similar to the result by Rafelski et al. (2011), and we compare the two studies in Section 5.1. We consider how the normalization k_3 of $f(N_{\mathrm{H\,I}}, X)$ affects the SFR efficiency in Section 5.2. We interpret the results and compare the results to predictions from models in Section 5.3. We also compare them to the SFR efficiency of local H I gas in Section 5.4, and to measurements from the double DLA

technique in Section 5.5. Lastly, we consider the effects of dust in Section 5.6.

5.1. Comparison to Rafelski et al. (2011)

We compare the SFR efficiency determined here at $z \sim 3$ to that previously measured by Rafelski et al. (2011) and find that the SFR efficiencies are very similar, although slightly lower than before. Specifically, Rafelski et al. (2011) find a mean efficiency of ~3.2%, while the new measurement is 2.8%. This is well within the ~1% spread in measurements that vary weakly as a function of the inferred gas surface density. The agreement is not surprising, given that the same technique was implemented in a somewhat overlapping data set. The key differences include the improved galaxy redshifts from Rafelski et al. (2015), the use of both the rest-frame FUV and NUV in the galaxy stacks, an updated $f(N_{\mathrm{H\,I}})$, and the higher sample completeness at fainter magnitudes.

Even though the improved galaxy redshifts found two catastrophic redshift errors in the Rafelski et al. (2011) sample, they did not significantly affect the stack since they are created from a median image. The update to $f(N_{\mathrm{H\,I}})$ at $z \sim 3$ was sufficiently small to be inconsequential. Lastly, the higher sample completeness results in less of a dependence on completeness corrections, but the previous corrections were sufficiently accurate that the updated values have not changed significantly.

5.2. Normalization of the Column-density Distribution Function

One of the largest uncertainties in the evolution of the SFR efficiency is the normalization k_3 of $f(N_{\mathrm{H\,I}})$ at $z \sim 1$. Since k_3 is currently not well measured at $z \sim 1$, we have to rely on linear fits with redshift as done in Section 3.1 to obtain two possible estimates of k_3 at $z = 1$. We note that these values of k_3 bracket the measurement at $z \sim 0.6$. Figure 9 and Table 2 show different SFR efficiencies at $z \sim 1$ depending on k_3, and we consider those differences here.

One method to obtain k_3 at $z \sim 1$ is to extrapolate between the $z = 0$ and $z \sim 2$ measurements, as done with the red dotted line in Figure 6. However, this relies heavily on the $z = 0$ value of k_3, and this value is highly uncertain as it depends on the shape of $f(N_{\mathrm{H\,I}})$ at $z = 0$, which is not well known. Specifically, two studies that measure it report highly discrepant shapes, especially at lower column densities (Zwaan et al. 2005; Braun 2012). Moreover, neither one of these shapes agrees well with that at $z > 2$, although the Zwaan et al. (2005) measurement is more similar than that by Braun (2012). Also, we note that the Braun (2012) measurements only use a few galaxies to constrain $f(N_{\mathrm{H\,I}})$.

The difference in the shape of $f(N_{\mathrm{H\,I}})$ in the two $z = 0$ studies is partially due to differences in the methodology used. It is unclear which method is more correct, and this translates into large systematic uncertainties in k_3 at $z = 0$. The measurement of $f(N_{\mathrm{H\,I}})$ at $z \sim 0.6$ is consistent with the $z > 2$ measurements and the Zwaan et al. (2005) measurement, but not with the Braun (2012) measurement at lower column densities (Neeleman et al. 2016).

We therefore measure k_3 at $z = 0$ by using the Zwaan et al. (2005) data to fit $f(N_{\mathrm{H\,I}})$, forcing the shape to match that at $z > 2$. This is not a good fit due to the shape disagreement, but it provides a reasonable estimate for k_3 of -24.07, which

corresponds to the red crosses in Figure 9. For this value of k_3 there is a slight decrease in the SFR efficiency of H I gas with decreasing redshift. We note that this is not possible with the Braun (2012) data, as the shape is too deviant from that at $z > 2$.

An alternative (and preferred) method is to obtain k_3 at $z \sim 1$ by a linear fit of the data including the $z = 0.6$ and $z > 2$ data together, as shown with the blue dashed line in Figure 6. This results in $k_3 = -24.21$, which corresponds to the blue diamonds in Figure 9. This result is also consistent with the measurement at $z \sim 0.6$ (Neeleman et al. 2016), although the higher-redshift data points are more heavily weighted due to the large uncertainty. An extrapolation of fitting just the $z > 2$ data yields $k_3 = -24.26$, which results in a very similar SFR efficiency and thus is not shown (but is tabulated in Table 2). This method of obtaining k_3 is likely more reliable than that obtained from the extrapolation to the highly uncertain measurement at $z = 0$, as it is based on measurements conducted in the same fashion. For this measurement of k_3, there is no observed evolution in the SFR efficiency of H I gas with redshift, and we consider it as our primary measurement of the SFR efficiency below.

5.3. Comparison with Models

Galaxy simulations incorporating H_2-regulated star formation find that the primary source for lower SFR efficiencies at high redshift is a decrease in the dust content, which is well traced by the metallicity of the gas (Gnedin & Kravtsov 2010; Kuhlen et al. 2012; Hopkins et al. 2014; Somerville et al. 2015). These simulations predict a reduced SFR efficiency for DLA gas due to their low metallicities. For instance, Gnedin & Kravtsov (2010) predict efficiencies matching those by Rafelski et al. (2011) at $z \sim 3$. The low dust content of DLAs, as traced by the metallicity, could therefore explain the reduced SFR efficiencies. In fact, studies of star formation at low metallicity in the Small Magellanic Cloud also find a lower SFR efficiency (Bolatto et al. 2011; Jameson et al. 2015).

We compare our results to the cosmological simulations by Gnedin & Kravtsov (2010) at $z \sim 3$ for gas with metallicity below $0.1\ Z_\odot$.[11] These simulations include a metallicity-dependent model of molecular hydrogen (Gnedin et al. 2009). Figure 12 shows that the Gnedin & Kravtsov (2010) simulations predict the same SFR efficiency as measured here. Gnedin & Kravtsov (2010) conclude that the lower metallicity, and therefore lower dust-to-gas ratio, causes a decrease in the amplitude of the KS relation, as observed here. Gnedin & Kravtsov (2010) also find that while the higher UV flux at high redshift does lower the SFR, it also lowers the surface density of the neutral gas, leaving the KS relation mostly unaffected.

Due to the limited redshift and metallicity range of these simulations, we cannot directly investigate the expected evolution as a function of redshift and metallicity. We therefore turn to analytic models. The KMT+ model by Krumholz (2013) explicitly computes the behavior of H I-dominated gas in the galaxy outskirts and provides us with the Σ_{SFR} as a function of the metallicity and Σ_{gas}. This model is based on the KMT slab model (Krumholz et al. 2008, 2009b, 2009c), which

---

[11] The metallicity cut of $0.1\ Z_\odot$ is reasonable, given that the mass-weighted and volume-weighted metallicity of atomic gas is ~$0.02\ Z_\odot$ and ~$0.03\ Z_\odot$, respectively (Rafelski et al. 2011).
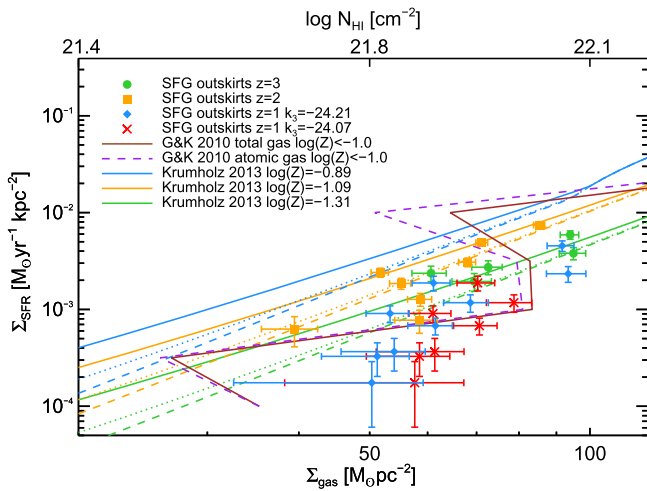
Figure 12. Comparison of the SFR efficiency of DLA gas in the outskirts of SFGs at $z \sim 1$–3 with the cosmological simulation at $z \sim 3$ by Gnedin & Kravtsov (2010) and the analytic KMT+ model by Krumholz (2013) for molecule-poor galaxies for different metallicities. The brown line is the mean relation for the total neutral-gas surface density (atomic and molecular) in the cosmological simulation, and the purple dashed line is the same for only atomic hydrogen gas. The KMT+ model predictions are for the metallicities of DLAs at the redshifts of the binned SFGs, with the colors matching those of the corresponding measurements at each redshift: green for $z = 3$, orange for $z = 2$, and blue for $z = 1$. The solid, dotted, and dashed lines use stellar densities of $0.1 \, M_\odot \, \mathrm{pc}^{-3}$, $0.01 \, M_\odot \, \mathrm{pc}^{-3}$, and $0.001 \, M_\odot \, \mathrm{pc}^{-3}$, respectively. The model provides a measure of the expected evolution in the SFR as a function of redshift due to the metallicity evolution of DLAs (Rafelski et al. 2012), which would evolve from the green line at $z = 3$ to the blue line at $z = 1$. Our measurements use the same symbols as in Figure 9, consisting of green circles, orange squares, blue diamonds, and red crosses, respectively. The data are broadly in agreement with the simulations and models, although the data do not reproduce the predicted metallicity evolution. Specifically, the blue diamonds and red crosses are predicted to fall on the blue line, and they fall significantly below and to the right, revealing no evolution with redshift and therefore metallicity.

resulted in a fixed ratio of the interstellar radiation field (ISRF) to gas density. The newer KMT+ model allows the ratio of ISRF to gas density to vary, which is necessary at low ISRF intensities to maintain hydrostatic equilibrium. This results in a floor on the density of cold H I gas and also results in a floor on the H$_2$ fraction and the SFR (Krumholz 2013).

The analytic model by Krumholz (2013) is able to reproduce the observed low efficiencies at the metallicities of DLAs. Moreover, the model can also be used to predict the expected Σ_{SFR} as a function of the Σ_{gas} at different metallicities and therefore redshifts. The metallicity of DLA gas increases with decreasing redshift, with a ~ 0.4 dex evolution from $z \sim 3$ to $z \sim 1$ ($\log(Z) = -1.31$ to $\log(Z) = -0.89$, where Z is the ratio of the metal to hydrogen column density normalized to solar; Rafelski et al. 2012, 2014). This translates to a change of ~ 0.5 dex in the Σ_{SFR}, assuming constant stellar densities (Krumholz 2013), as shown in Figure 12. While this level of evolution can be measured with the precision of our measurements, we find no evolution in the SFR efficiency of atomic-dominated H I gas. While the model is somewhat consistent with the evolution observed from $z \sim 3$ to $z \sim 2$, the $z \sim 1$ points fall significantly below and to the right of the model. This is true regardless of the value of k_3 used in $f(N_{\mathrm{H\,I}})$ at $z \sim 1$.

Besides gas densities and metallicity, stellar density is an additional parameter that in some models (e.g., McKee & Ostriker 2007) regulates the SFR, although they are unknown

for DLAs. To gauge the importance of stellar density, we turn again to the model by Krumholz (2013), computing the expected SFR for three values of the stellar density, 0.1, 0.01, and $0.001 \, M_\odot \, \mathrm{pc}^{-3}$. The local neighborhood has stellar densities of $0.01 \, M_\odot \, \mathrm{pc}^{-3}$ (Holmberg & Flynn 2000), and increasing or decreasing the stellar density does not alter our conclusions substantially as shown in Figure 12. In addition, the gas surface densities are sufficiently high such that the stellar gravity is a small contribution to the total pressure, and therefore they should have small effects on the resultant SFR efficiencies (Krumholz 2013). These surface densities are also unlikely to evolve significantly from $z \sim 2$ to $z \sim 1$.

In the KMT+ model, the FUV background is dominated by the local star formation rather than the cosmic FUV background (Haardt & Madau 2012; Krumholz 2013), and the FUV field and SFR are computed self-consistently. Therefore, any feedback effects caused by the decreased UV radiation from the lower SFR efficiency as a function of metallicity are already built into the model. However, this depends on whether we truly understand the interplay between the metallicity and the UV background, and how the two play off each other in cosmological simulations (e.g., Gnedin & Kravtsov 2010, 2011; Somerville et al. 2015). For instance, if the FUV radiation field is not dominated by local star formation, but rather by cosmic FUV background, then it may be possible that the lack of evolution could be caused by a balance of an increased efficiency of higher-metallicity gas canceled by the lower efficiency of a higher cosmic FUV background. However, this is not currently predicted by models.

There are many uncertainties in how we implement the UV background in models and simulations, which would affect the amplitude of the UV background. Moreover, we do not fully understand the interplay between the metallicity and the UV background, and how the two play off each other in a cosmological context (R. Somerville 2016, private communication). Further investigations with cosmological simulations are warranted, and such simulations would need to reproduce our observed lack of evolution in the SFR efficiency with redshift and metallicity from $z \sim 1$ to 3.

One possibility that could affect the SFR efficiency comparison is if we had to exclude from our analysis a population of "low-cool" DLAs (Wolfe et al. 2008), i.e., a subset of DLAs that are believed to be unrelated to ongoing star formation. Excluding low-cool DLAs would decrease the number of DLAs (or equivalently reduce the value for $f(N_{\mathrm{H\,I}}, X)$), yielding a lower $d\dot{\rho}_*/d\langle I_{\nu_0}^{\mathrm{obs}}\rangle$. In Rafelski et al. (2011) we find that this decrease would result in a ~ 0.1 dex shift to the left in the inferred Σ_{gas} in Figure 12, which also brings the measurements into somewhat better agreement with the model. While no redshift evolution of this bimodality is likely (Wolfe et al. 2008), even such an evolution would not be sufficient to change our result to an evolution in the SFR efficiency with redshift.

5.4. Comparison with Local Data

An alternative explanation for the reduced SFR efficiency is the role of molecular versus atomic hydrogen gas in star formation. Empirically, the Σ_{SFR} of local spiral galaxies is well correlated with the $\Sigma_{\mathrm{H_2}}$ (e.g., Bigiel et al. 2008, 2011), and some have argued that the KS relation is only valid for molecular-dominated gas rather than for atomic-dominated gas (e.g., Wong & Blitz 2002; Schruba et al. 2011). However, an
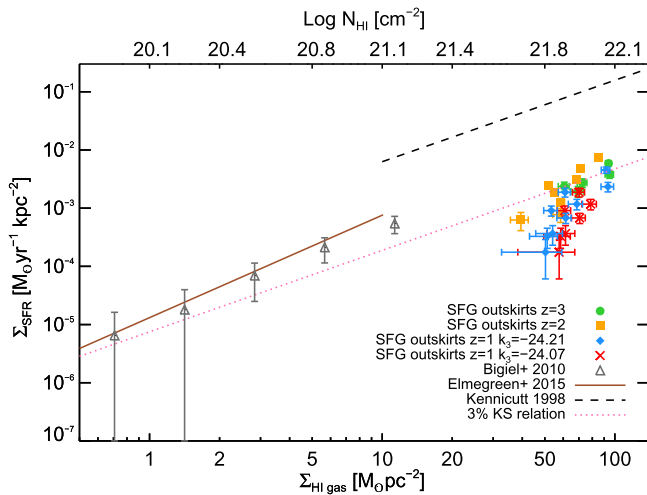
Figure 13. Comparison of the SFR efficiency of DLA gas in the outskirts of SFGs at $z \sim 1$–3 with local measurements. This shows that the local spiral galaxy outskirts and dwarf galaxies have a similar reduced SFR efficiency to that measured here statistically in DLAs. The pink dotted line represents the KS relation at 3% efficiency, which is consistent with our measurements and similar to the local measurements, although slightly lower. Our measurements again use the same symbols as in Figure 9, consisting of green circles, orange squares, blue diamonds, and red crosses. The gray triangles are for the outskirts of local spiral galaxies (Bigiel et al. 2010b), the brown line is for local dwarf galaxies (Elmegreen & Hunter 2015), and the black line represents the KS relation (Kennicutt 1998b).

analysis of the atomic-dominated gas in the outskirts of spiral galaxies reveals a clear correlation of the Σ_{SFR} and the $\Sigma_{H\,I}$ (Bigiel et al. 2010a, 2010b; Roychowdhury et al. 2015). Similarly, atomic-dominated dwarf galaxies also have a clear correlation of the Σ_{SFR} with the $\Sigma_{H\,I}$ (Roychowdhury et al. 2014; Elmegreen & Hunter 2015).

We do not assert that stars form directly out of atomic-dominated H I gas, and our measurements do not distinguish or depend on whether the atomic hydrogen gas transitions to the molecular phase before forming stars. However, some simulations show that gas without H_2 or CO can cool to low enough temperatures to form stars by gravitational collapse (Glover & Mac Low 2011; Glover & Clark 2012). Similarly, observations of some GRB host galaxies suggest that star formation may be directly fueled by atomic gas (Michałowski et al. 2015). The H_2 observed at low metallicity may therefore be a consequence of star formation, rather than the cause. It is very difficult to measure H_2 in these regimes, since much of this H_2 may be CO-dark (Wolfire et al. 2010), and the covering fraction of H_2 may be lower than that of H I. Even so, we expect that there will be some molecular gas present in these atomic-dominated regimes (Schruba et al. 2011), and it is even observed directly in one low-metallicity dwarf galaxy (Leroy et al. 2006).

DLAs have a sufficiently high column density of H I gas that the gas is self-shielded (Wolfe et al. 2005), which could allow star formation even with low levels of dust. The main constraint for DLA gas is that molecular hydrogen has a very small cross section due to either a lack of molecular hydrogen in the gas, the fact that the molecular phase is present over only a short timescale, or the fact that the volume filling fraction is small, since most DLAs do not show evidence of abundant H_2 based on the Lyman and Werner transitions (Jorgenson et al. 2014; Noterdaeme et al. 2015a).

Figure 13 compares the SFR efficiency measured in DLA gas in the outskirts of SFGs to that of the H I gas in the outskirts

of local spiral (Bigiel et al. 2010b, gray triangles) and dwarf galaxies (Elmegreen & Hunter 2015, brown line) and shows a reduced SFR efficiency in atomic-dominated H I gas compared to the KS relation, shown as the black dashed line. These measurements at $z = 0$ show SFR efficiencies similar (slightly higher) to those presented here at $z \sim 1$–3 (e.g., pink dotted line in Figure 13), suggesting that perhaps the efficiency of this gas is not changing significantly over time or strongly with metallicity.

The similar efficiency of H I-dominated gas at both low and high redshift and at different metallicities shown in Figure 13, combined with the lack of any observed evolution in the efficiency of DLAs as a function of redshift (and therefore metallicity), suggests that the reduced SFR efficiency is likely driven by the low molecular content of the atomic-dominated phase. At the same time, the metallicity could play a secondary effect on the efficiency by regulating the conversion between atomic and molecular gas. Theory predicts that there is a metallicity dependence on this transition (Krumholz et al. 2009b), which would explain the observed high column densities of DLAs without much molecular gas. In this scenario, the metallicity of the DLA gas is too low for the atomic gas to form significant amounts of molecular gas at the given surface densities. This may explain how the KMT+ model does not reproduce the lack of evolution in the efficiency of the DLA gas, while at the same time reproducing the SFR efficiency of the local H I gas (Krumholz 2013). We note that our data do not directly constrain the metallicity dependence of the transition to the molecular phase. Rather, we add constraints for future models and simulations by providing measurements that show no strong evolution in the SFR efficiency as a function of metallicity.

5.5. Comparison with Double DLA Measurements

The dependence of the H I-to-H_2 transition on metallicity, coupled with the typically higher metallicity at $z = 0$, suggests that it is unlikely that we will measure H I gas locally at the surface densities of the high-column-density DLA gas measured here. However, it is possible to measure the SFRs of DLAs at lower column densities at high redshift using the double DLA technique described in Section 1. This technique was used to search for emission from typical DLAs at $z \sim 2$–3 (Fumagalli et al. 2010, 2014, 2015), and no emission from the DLAs was detected.

The upper limits of these measurements for *HST* and ground-based observations are shown as purple and gold bowties in Figure 14. In addition, these measurements were stacked to improve S/N, shown as the solid purple and gold horizontal bars. The *HST* and ground-based measurements cannot be combined, as they measure star formation over different areas matched to the resolution of the images. We note that these measurements determine Σ_{SFR} over a specific area, and these values could be higher if star formation is occurring only in regions smaller than these apertures, which are matched to the resolution of the telescopes. Also, we note that these limits are not corrected for inclination.

The resulting upper limits are consistent with both the measurements presented here and those of local spiral and dwarf galaxies. However, the sensitivities are not sufficient to yield strong constraints on the SFR efficiency of the gas. Also, we note that the results and model from this study are consistent with the results in Fumagalli et al. (2015), as the
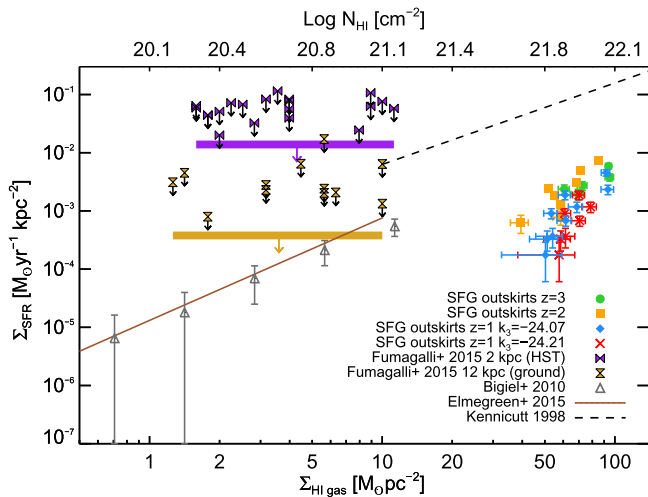
Figure 14. Comparison of the SFR efficiency of DLA gas in the outskirts of SFGs at $z \sim 1$–3 with local measurements and lower-column-density DLA gas via the double DLA technique. This shows that the upper limits from direct DLA observations are consistent with both our measurements and the local H I gas. The upper limits of DLAs at $z \sim 2$–3 for *HST* and ground-based observations are shown as purple and gold bowties, respectively (Fumagalli et al. 2015). Our measurements use the same symbols as in Figure 9, consisting of green circles, orange squares, blue diamonds, and red crosses. The gray triangles are for the outskirts of local spiral galaxies (Bigiel et al. 2010b), the brown line is for local dwarf galaxies (Elmegreen & Hunter 2015), and the black line represents the KS relation (Kennicutt 1998b).

galaxies studied here are for the most part below their sensitivity level. Measurements at higher H I column densities with higher sensitivities would enable a direct comparison with the results from this study and are likely to result in direct detections of typical DLAs. This would in turn result in a more direct measurement of the SFR efficiency of atomic-dominated H I gas at high redshift.

5.6. Possible Dust Extinction

The rest-frame FUV light from normal high-redshift SFGs suffers from dust extinction by a factor of up to five (Reddy et al. 2012), which could reduce our measured SFR efficiency. However, in the outskirts of local galaxies, Bigiel et al. (2010b) find that the FUV emission reflects the recently formed stars without large biases from external extinction. We similarly do not expect much extinction in the outer parts of the SFGs, as DLAs have low dust-to-gas ratios and low levels of extinction (Murphy & Liske 2004; Frank & Péroux 2010; Khare et al. 2012; Fukugita & Ménard 2015; Murphy & Bernet 2016).

Regardless, if we consider the unlikely scenario in which the maximum extinction were present in the outskirts, the SFR efficiency would still not be close to the expected value, and the reduced SFR efficiencies would remain. Specifically, a factor of five in extinction would raise the SFR efficiencies by approximately a factor of five as well, resulting in efficiencies of $\lesssim 20\%$. However, this is unlikely since the dust is concentrated in the center of the galaxies (Nelson et al. 2016).

Another unlikely possibility to consider is if dust extinction could cause us to miss an evolution with redshift. This would require that the outskirts of $z \sim 1$ SFGs have more dust than the $z \sim 2$ or $z \sim 3$ SFGs. To test this possibility, we artificially added extinction to the $z \sim 1$ stack and find that a minimum of ~ 1 mag extra extinction over that at $z \sim 2$ would be necessary to make the measurements consistent with a metallicity

evolution, and an extinction of ~ 3 mag would be needed to clearly show an evolution with redshift. This assumes that $\log k_3 = -24.26$, while $\log k_3 = -24.07$ would require even more extinction.

It is extremely unlikely that the extinction in the outskirts of these galaxies would evolve so drastically from $z \sim 2$ to $z \sim 1$, especially given the low levels of extinction measured in DLAs at similar redshifts. While there is a small spread in the reddening caused by DLAs, the most recent measurements find $E(B - V) = 0.003$ mag (Murphy & Bernet 2016), while the highest measurement is $E(B - V) = 0.01$ mag (Fukugita & Ménard 2015). We note that while the extinction is correlated with the metallicity of DLAs, it is uncorrelated with $N_{\mathrm{H\,I}}$ (Murphy & Bernet 2016), which is consistent with the finding that $N_{\mathrm{H\,I}}$ in DLAs is uncorrelated with the metallicity of DLAs (Neeleman et al. 2013). We therefore conclude that dust extinction does not affect our results.

6. SUMMARY

Measurements of the evolution in the SFR efficiency of neutral atomic-dominated hydrogen gas are needed to understand the origin of the reduced SFR efficiency measured at $z \sim 3$ (Wolfe & Chen 2006; Rafelski et al. 2011). Here we present the SFR efficiency of this gas at $z \sim 1$, $z \sim 2$, and $z \sim 3$ measured in the outskirts of SFGs, assuming that DLAs are associated with SFGs and that the outskirts of these galaxies are composed of H I gas. These assumptions are well warranted, given the significant evidence for the association of DLAs with SFGs and the covering fractions of the outskirts of these galaxies compared to the molecular- and atomic-dominated gas (Figures 10 and 11).

We select SFGs in the UDF at $z \sim 1$, $z \sim 2$, and $z \sim 3$ using new photometric redshifts from Rafelski et al. (2015) utilizing new UV imaging of the UDF, and we create composite image stacks of isolated, compact, and symmetric SFGs in the rest-frame UV. We extract radial surface brightness profiles (Figure 4), which show low surface brightness emission out to large radii (~ 8 kpc). This emission is interpreted as in situ star formation in H I gas surrounding the SFGs.

In order to obtain the SFR efficiency, we require $f(N_{\mathrm{H\,I}})$, and we fit a double power law to the number of high-density absorbers to background quasars at $z \sim 2$–3.5 using the data from Noterdaeme et al. (2012) combined with the $z = 0.6$ data from Neeleman et al. (2016) to determine the evolution of the normalization k_3 as a function of redshift. In addition, we consider a second value of k_3 by interpolating between the $z \sim 2$ value and the $z \sim 0$ value obtained by fitting double power law to the data from Zwaan et al. (2005), requiring the same shape. Figure 6 shows the evolution for both possible values of k_3, and we consider both possibilities for k_3 when determining the SFR efficiency.

We determine the SFR efficiency of atomic-dominated hydrogen gas at each redshift by comparing the emission in the outskirts of SFGs to that expected from the Rafelski et al. (2011) model, which is based on the KS relation and $f(N_{\mathrm{H\,I}})$ (see Figure 7). The resulting SFR efficiencies are similar to those found at $z \sim 3$ by Rafelski et al. (2011). The SFR efficiency is then combined with the measured Σ_{SFR} to visualize the results on the familiar KS relation plot (Figure 8). We directly compare the SFR efficiencies at different redshifts to each other as a function of their inferred Σ_{gas} to investigate

any evolution in the efficiency (Figure 9), and we find no evolution with redshift.

Given the success of models and simulations using H_2-regulated star formation in reproducing the reduced SFR efficiency of the H I gas at $z \sim 3$ (Gnedin & Kravtsov 2010; Krumholz 2013), the expectation was that the SFR efficiency would evolve with the metallicity. The metallicity of DLA gas increases with decreasing redshift, with a ~ 0.4 dex evolution from $z \sim 1$ to $z \sim 3.0$ (Rafelski et al. 2012, 2014), which would be more than sufficient to measure an increase in the SFR efficiency of the gas (Figure 12). However, the lack of any evolution of the SFR efficiency with redshift instead suggests that it may be driven by the low molecular content of this atomic-dominated phase. The metallicity may instead play a secondary effect in regulating the conversion between atomic and molecular gas. This interpretation is supported by the similar SFR efficiency observed in H I gas at $z = 0$ in the outskirts of spiral galaxies (Bigiel et al. 2010b) and dwarf galaxies (Elmegreen & Hunter 2015) (Figure 13).

We compare the results measured statistically here to direct measurements of individual DLAs using the double DLA technique (Fumagalli et al. 2015). We find that the two results are consistent with each other, as the direct measurements are all upper limits at lower H I column densities (Figure 14). A more direct comparison would be possible with deep UV imaging targeting higher-column-density gas using the double DLA technique. Such observations are currently possible with WFC3/UVIS on *HST* and would verify the results presented here and yield the first direct imaging of a typical DLA unbiased by metallicity.

REFERENCES

Ahn, C. P., Alexandroff, R., Allende Prieto, C., et al. 2012, ApJS, 203, 21
Alavi, A., Siana, B., Richard, J., et al. 2014, ApJ, 780, 143
Amorin, R., Muñoz-Tuñón, C., Aguerri, J. A. L., et al. 2016, A&A, 588, A23
Beckwith, S. V. W., Stiavelli, M., Koekemoer, A. M., et al. 2006, AJ, 132, 1729
Benítez, N. 2000, ApJ, 536, 571
Bertin, E., & Arnouts, S. 1996, A&AS, 117, 393
Bielby, R., Hill, M. D., Shanks, T., et al. 2013, MNRAS, 430, 425
Bigiel, F., Leroy, A., Seibert, M., et al. 2010a, ApJL, 720, L31
Bigiel, F., Leroy, A., Walter, F., et al. 2008, AJ, 136, 2846
Bigiel, F., Leroy, A., Walter, F., et al. 2010b, AJ, 140, 1194
Bigiel, F., Leroy, A. K., Walter, F., et al. 2011, ApJL, 730, L13
Bird, S., Vogelsberger, M., Haehnelt, M., et al. 2014, MNRAS, 445, 2313
Boissier, S., Gil de Paz, A., Boselli, A., et al. 2008, ApJ, 681, 244
Bolatto, A. D., Leroy, A. K., Jameson, K., et al. 2011, ApJ, 741, 12
Bolatto, A. D., Wolfire, M., & Leroy, A. K. 2013, ARA&A, 51, 207
Bouché, N., Murphy, M. T., Kacprzak, G. G., et al. 2013, Sci, 341, 50
Bouwens, R. J., Illingworth, G. D., Oesch, P. A., et al. 2011, ApJ, 737, 90
Bouwens, R. J., Illingworth, G. D., Oesch, P. A., et al. 2015, ApJ, 803, 34
Braun, R. 2012, ApJ, 749, 87
Cen, R. 2012, ApJ, 748, 121
Cooke, J., Wolfe, A. M., Gawiser, E., et al. 2006, ApJL, 636, L9
Crighton, N. H. M., Murphy, M. T., Prochaska, J. X., et al. 2015, MNRAS, 452, 217
Cucchiara, A., Fumagalli, M., Rafelski, M., et al. 2015, ApJ, 804, 51
Daddi, E., Elbaz, D., Walter, F., et al. 2010, ApJL, 714, L118
Ellis, R. S., McLure, R. J., Dunlop, J. S., et al. 2013, ApJL, 763, L7
Elmegreen, B. G., & Hunter, D. A. 2015, ApJ, 805, 145
Elmegreen, B. G., Rubio, M., Hunter, D. A., et al. 2013, Natur, 495, 487
Font-Ribera, A., Miralda-Escude, J., Arnau, E., et al. 2012, JCAP, 11, 059
Frank, S., & Péroux, C. 2010, MNRAS, 406, 2235
Fukugita, M., & Ménard, B. 2015, ApJ, 799, 195
Fumagalli, M., & Gavazzi, G. 2008, A&A, 490, 571
Fumagalli, M., O'Meara, J. M., Prochaska, J. X., et al. 2010, MNRAS, 408, 362
Fumagalli, M., O'Meara, J. M., Prochaska, J. X., et al. 2014, MNRAS, 444, 1282
Fumagalli, M., O'Meara, J. M., Prochaska, J. X., et al. 2015, MNRAS, 446, 3178
Fynbo, J. P. U., Geier, S. J., Christensen, L., et al. 2013, MNRAS, 436, 361
Fynbo, J. P. U., Laursen, P., Ledoux, C., et al. 2010, MNRAS, 408, 2128
Genzel, R., Tacconi, L. J., Gracia-Carpio, J., et al. 2010, MNRAS, 407, 2091
Glover, S. C. O., & Clark, P. C. 2012, MNRAS, 421, 9
Glover, S. C. O., & Mac Low, M.-M. 2011, MNRAS, 412, 337
Gnedin, N. Y., & Kravtsov, A. V. 2010, ApJ, 714, 287
Gnedin, N. Y., & Kravtsov, A. V. 2011, ApJ, 728, 88
Gnedin, N. Y., Tassis, K., & Kravtsov, A. V. 2009, ApJ, 697, 55
Grogin, N. A., Kocevski, D. D., Faber, S. M., et al. 2011, ApJS, 197, 35
Haardt, F., & Madau, P. 2012, ApJ, 746, 125
Hathi, N. P., Jansen, R. A., Windhorst, R. A., et al. 2008, AJ, 135, 156
Helfer, T. T., Thornley, M. D., Regan, M. W., et al. 2003, ApJS, 145, 259
Henry, A., Scarlata, C., Martin, C. L., et al. 2015, ApJ, 809, 19
Holmberg, J., & Flynn, C. 2000, MNRAS, 313, 209
Hopkins, P. F., Kereš, D., Onorbe, J., et al. 2014, MNRAS, 445, 581
Illingworth, G. D., Magee, D., Oesch, P. A., et al. 2013, ApJS, 209, 6
Jameson, K. E., Bolatto, A. D., Leroy, A. K., et al. 2015, ApJ, in press (arXiv:1510.08084)
Jorgenson, R. A., Murphy, M. T., Thompson, R., et al. 2014, MNRAS, 443, 2783
Jorgenson, R. A., & Wolfe, A. M. 2014, ApJ, 785, 16
Kennicutt, R. C. 1998a, ARA&A, 36, 189
Kennicutt, R. C. 1998b, ApJ, 498, 541
Kennicutt, R. C., & Evans, N. J. 2012, ARA&A, 50, 531
Khare, P., Vanden Berk, D., York, D. G., et al. 2012, MNRAS, 419, 1028
Koekemoer, A. M., Ellis, R. S., McLure, R. J., et al. 2013, ApJS, 209, 3
Koekemoer, A. M., Faber, S. M., Ferguson, H. C., et al. 2011, ApJS, 197, 36
Krogager, J.-K., Fynbo, J. P. U., Ledoux, C., et al. 2013, MNRAS, 433, 3091
Krogager, J. K., Fynbo, J. P. U., Møller, P., et al. 2012, MNRAS, 424, L1
Kroupa, P., & Weidner, C. 2003, ApJ, 598, 1076
Krumholz, M. R. 2012, ApJ, 759, 9
Krumholz, M. R. 2013, MNRAS, 436, 2747
Krumholz, M. R., Ellison, S. L., Prochaska, J. X., et al. 2009a, ApJL, 701, L12
Krumholz, M. R., McKee, C. F., & Tumlinson, J. 2008, ApJ, 689, 865
Krumholz, M. R., McKee, C. F., & Tumlinson, J. 2009b, ApJ, 693, 216
Krumholz, M. R., McKee, C. F., & Tumlinson, J. 2009c, ApJ, 699, 850
Kuhlen, M., Krumholz, M. R., Madau, P., et al. 2012, ApJ, 749, 36
Kumar, P., & Zhang, B. 2015, PhR, 561, 1
Lagos, C. D. P., Baugh, C. M., Lacey, C. G., et al. 2011, MNRAS, 418, 1649
Lagos, C. D. P., Baugh, C. M., Zwaan, M. A., et al. 2014, MNRAS, 440, 920
Langer, W. D., Velusamy, T., Pineda, J. L., et al. 2014, A&A, 561, A122
Leroy, A., Bolatto, A., Walter, F., et al. 2006, ApJ, 643, 825
Leroy, A. K., Bolatto, A., Gordon, K., et al. 2011, ApJ, 737, 12
McKee, C. F., & Ostriker, E. C. 2007, ARA&A, 45, 565
Michałowski, M. J., Gentile, G., Hjorth, J., et al. 2015, A&A, 582, A78
Møller, P., Warren, S. J., & Fall, S. M. 2002, ApJ, 574, 51
Murphy, M. T., & Bernet, M. L. 2016, MNRAS, 455, 1043
Murphy, M. T., & Liske, J. 2004, MNRAS, 354, L31
Muzzin, A., Marchesini, D., Stefanon, M., et al. 2013, ApJ, 777, 18
Nagamine, K., Wolfe, A. M., Hernquist, L., et al. 2007, ApJ, 660, 945
Neeleman, M., Prochaska, J. X., Ribaudo, J., et al. 2016, ApJ, 818, 113
Neeleman, M., Wolfe, A. M., Prochaska, J. X., et al. 2013, ApJ, 769, 54
Nelson, E. J., van Dokkum, P. G., Momcheva, I. G., et al. 2016, ApJL, 817, L9
Noterdaeme, P., Petitjean, P., Carithers, W. C., et al. 2012, A&A, 547, L1
Noterdaeme, P., Petitjean, P., Ledoux, C., et al. 2009, A&A, 505, 1087
Noterdaeme, P., Petitjean, P., & Pâris, I. 2014, A&A, 566, A24

Noterdaeme, P., Petitjean, P., & Srianand, R. 2015a, A&A, 578, L5
Noterdaeme, P., Srianand, R., Rahmani, H., et al. 2015b, A&A, 577, A24
Obreschkow, D., & Rawlings, S. 2009, ApJL, 696, L129
Oesch, P. A., Bouwens, R. J., Carollo, C. M., et al. 2010a, ApJL, 709, L21
Oesch, P. A., Bouwens, R. J., Carollo, C. M., et al. 2010b, ApJL, 725, L150
Oesch, P. A., Bouwens, R. J., Illingworth, G. D., et al. 2010c, ApJL, 709, L16
O'Meara, J. M., Chen, H.-W., & Kaplan, D. L. 2006, ApJL, 642, L9
Péroux, C., Bouché, N., Kulkarni, V. P., et al. 2012, MNRAS, 419, 3060
Péroux, C., Quiret, S., Rahmani, H., et al. 2016, MNRAS, 457, 903
Pirzkal, N., Sahu, K. C., Burgasser, A., et al. 2005, ApJ, 622, 319
Pontzen, A., Governato, F., Pettini, M., et al. 2008, MNRAS, 390, 1349
Popping, G., Somerville, R. S., & Trager, S. C. 2014, MNRAS, 442, 2398
Prochaska, J. X., Gawiser, E., Wolfe, A. M., et al. 2003, ApJL, 595, L9
Prochaska, J. X., Herbert-Fort, S., & Wolfe, A. M. 2005, ApJ, 635, 123
Prochaska, J. X., & Wolfe, A. M. 2009, ApJ, 696, 1543
Rafelski, M., Neeleman, M., Fumagalli, M., et al. 2014, ApJL, 782, L29
Rafelski, M., Teplitz, H. I., Gardner, J. P., et al. 2015, AJ, 150, 31
Rafelski, M., Wolfe, A. M., & Chen, H.-W. 2011, ApJ, 736, 48
Rafelski, M., Wolfe, A. M., Cooke, J., et al. 2009, ApJ, 703, 2033
Rafelski, M., Wolfe, A. M., Prochaska, J. X., et al. 2012, ApJ, 755, 89
Reddy, N., Dickinson, M., Elbaz, D., et al. 2012, ApJ, 744, 154
Reddy, N. A., & Steidel, C. C. 2009, ApJ, 692, 778
Roychowdhury, S., Chengalur, J. N., Kaisin, S. S., et al. 2014, MNRAS, 445, 1392
Roychowdhury, S., Huang, M.-L., Kauffmann, G., et al. 2015, MNRAS, 449, 3700
Salpeter, E. E. 1955, ApJ, 121, 161
Sánchez-Ramírez, R., Ellison, S. L., Prochaska, J. X., et al. 2016, MNRAS, 456, 4488

Sargent, M. T., Daddi, E., Bethermin, M., et al. 2014, ApJ, 793, 19
Schaye, J. 2001, ApJL, 562, L95
Schiminovich, D., Ilbert, O., Arnouts, S., et al. 2005, ApJL, 619, L47
Schmidt, M. 1959, ApJ, 129, 243
Schruba, A., Leroy, A. K., Walter, F., et al. 2011, AJ, 142, 37
Schulze, S., Fynbo, J. P. U., Milvang-Jensen, B., et al. 2012, A&A, 546, A20
Shapley, A. E., Steidel, C. C., Pettini, M., et al. 2003, ApJ, 588, 65
Somerville, R. S., Popping, G., & Trager, S. C. 2015, MNRAS, 453, 4337
Steidel, C. C., Bogosavljević, M., Shapley, A. E., et al. 2011, ApJ, 736, 160
Steidel, C. C., & Hamilton, D. 1992, AJ, 104, 941
Tacconi, L. J., Genzel, R., Neri, R., et al. 2010, Natur, 463, 781
Tacconi, L. J., Neri, R., Genzel, R., et al. 2013, ApJ, 768, 74
Teplitz, H. I., Rafelski, M., Kurczynski, P., et al. 2013, AJ, 146, 159
Tescari, E., Viel, M., Tornatore, L., et al. 2009, MNRAS, 397, 411
Thilker, D. A., Bianchi, L., Meurer, G., et al. 2007, ApJS, 173, 538
Walter, F., Decarli, R., Sargent, M., et al. 2014, ApJ, 782, 79
Warren, S. J., Møller, P., Fall, S. M., et al. 2001, MNRAS, 326, 759
Wolfe, A. M., & Chen, H.-W. 2006, ApJ, 652, 981
Wolfe, A. M., Gawiser, E., & Prochaska, J. X. 2003a, ApJ, 593, 235
Wolfe, A. M., Gawiser, E., & Prochaska, J. X. 2005, ARA&A, 43, 861
Wolfe, A. M., Prochaska, J. X., & Gawiser, E. 2003b, ApJ, 593, 215
Wolfe, A. M., Prochaska, J. X., Jorgenson, R. A., et al. 2008, ApJ, 681, 881
Wolfire, M. G., Hollenbach, D., & McKee, C. F. 2010, ApJ, 716, 1191
Wong, T., & Blitz, L. 2002, ApJ, 569, 157
Zwaan, M. A., Meyer, M. J., Staveley-Smith, L., et al. 2005, MNRAS, 359, L30
Zwaan, M. A., & Prochaska, J. X. 2006, ApJ, 643, 675